CrossMark

Renewal of Transient Spiral Modes in Disk Galaxies

S. Sridhar

Raman Research Institute, Sadashivanagar, Bangalore 560 080, India; ssridhar@rri.res.in

Abstract

Spiral structure in disk galaxies could arise from transient modes that create conditions conducive for their regeneration; this is the proposal of Sellwood and Carlberg, based on simulations of stellar disks. The linear response of an axisymmetric stellar disk, to an adiabatic nonaxisymmetric transient mode, gives a final distribution function (DF) that is equal to the initial DF everywhere in phase space, except at the Lindblad and corotation resonances where the final DF is singular. We use the nonlinear theory of adiabatic capture into resonance to resolve the singularities and calculate the finite changes in the DF. These take the form of axisymmetric "scars" concentrated around resonances, whose DFs have simple general forms. Global changes in the physical properties are explored for a cool Mestel disk: we calculate the DFs of scars and estimate the changes in the disk angular momentum, surface density, and orbital frequencies leading to shifts in resonances. Resonant torques between disk stars and any new linear nonaxisymmetric mode are suppressed within a scar, as is epicyclic heating. Because all resonances of a linear mode with the same angular wavenumber and pattern speed as its precursor lie inside the scars of the precursor, it suffers less damping. Hence, scars filter the spectrum of noise-generated modes, promoting the renewal of a few select modes. Relic scars sustained by a galaxy disk, due to past tidal interaction with a passing companion, may still be active enablers of nonaxisymmetric modes, such as the two-armed "grand design" spiral patterns.

Key words: galaxies: kinematics and dynamics – galaxies: spiral – Galaxy: disk – Galaxy: kinematics and dynamics

1. Introduction

The spiral structure of disk galaxies is presumably caused by density waves, the origin and maintenance of which have been discussed for a long time; see, e.g., the reviews by Toomre (1977), Athanassoula (1984), Bertin & Lin (1996), Binney & Tremaine (2008), Sellwood (2014), and Shu (2016). It has been argued that a spiral density wave could be a quasi-stationary mode of an underlying smooth axisymmetric disk of stars and gas (Lin & Shu 1966; Bertin & Lin 1996; Shu 2016), but there is not much support for this notion from either linear perturbation theory or numerical simulations of initially axisymmetric stellar disks with a smooth distribution of stars in phase space (see Sellwood 2014 and references therein). In a purely stellar disk, the wave decays due to the excitation of the epicyclic oscillations ("heat") of disk stars, accompanying angular momentum transport across the disk. As the disk heats up, it becomes less efficient at sustaining the nonaxisymmetric mode. When gas is also present, energy is dissipated through shocks in the perturbed gas flow. Even though the gas mass is smaller than the stellar mass, it is important for the secular evolution of the disk through new star formation.

A tightly wound spiral density wave packet in a $Q \geqslant 1$ stellar disk propagates inside/outside the corotation resonance (CR) radius with the inner/outer radial boundary located at the inner and outer Lindblad resonances (ILR/OLR), where it is absorbed as a short trailing wave (Toomre 1969; Mark 1974). A more global approach considers a spiral perturbation (a spiral "mode") of fixed spatial form and pattern speed but with a time-varying amplitude. Lynden-Bell & Kalnajs (1972) showed that a nonaxisymmetric perturbation extracts angular momentum from the disk stars at the ILR and deposits it at the OLR, while heating up stars at both Lindblad resonances. There is no heating at the CR but angular momentum exchange

can be of either sign, causing radial mixing of stellar orbits (Sellwood & Binney 2002). A spiral density wave can undergo swing amplification as it unwinds from a leading to a trailing one, but this is a transient phenomenon (Goldreich & Lynden-Bell 1965; Julian & Toomre 1966; Toomre 1981). Global numerical linear theory computations by Toomre and Zang (Toomre 1981) displayed striking swing amplification of an initial leading spiral wave packet localized near the ILR. But this growth is transitory, and the wave unwinds until it is absorbed as a short, trailing wave packet at the ILR. The "local" (e.g., Toomre 1969) and "global" (Lynden-Bell & Kalnajs 1972) linear theory calculations are complementary points of view of the same physical process. In the former, the focus is on the conservation of the radial flux of angular momentum, which is the sum of the fluxes due to gravitational torques and advection, in the regions between the CR and ILR/OLR. In the latter, the focus is on the total angular momentum budget, with lasting exchanges occurring only at the resonances.

Transient spiral patterns appear abundantly in numerical simulations of stellar disks (see, e.g., Miller et al. 1970; Hockney & Brownrigg 1974; James & Sellwood 1978; Sellwood & Carlberg 1984; Sellwood & Lin 1989; Roškar et al. 2012), produced by swing amplification of shot noise. They have the intriguing property that they can be reborn, a line of thought that goes back to Sellwood & Carlberg (1984) and Sellwood (1989). As noted in Sellwood (2012, p. 2), "...the decay of one spiral feature might change the back-ground disk in such a manner as to create conditions for a new instability...." The transient patterns are mode like, with approximately constant spatial form and pattern speed but time-varying amplitudes; complex patterns seen in the simulations could be superpositions of a few spiral modes (Sellwood & Carlberg 2014, hereafter SC14). The dynamical origins of this

phenomenon, explored over decades of numerical simulations, are our central concern.

Plan of the paper: spiral perturbations mainly affect in-plane stellar motions, so we focus on planar dynamics, as has much of the essential analytical and numerical work in this field cited above. In Section 2, we discuss the decay of linear modes of a smooth axisymmetric distribution function (DF) from the point of view of Lynden-Bell & Kalnajs (1972). The emphasis is on the angular momentum transfer at the Lindblad and CRs, with the associated excitation of epicyclic motions. In Section 3, we take up the problem of the DF changes due to the passage of a single nonaxisymmetric transient mode on an unperturbed, axisymmetric galactic disk. Linear response theory (Carlberg & Sellwood 1985) predicts that, for an adiabatically varying transient, the change in the DF is singular at resonances. We use the nonlinear theory of adiabatic capture into resonance (Sridhar & Touma 1996, hereafter ST96) to resolve the singularities. The posttransient (or final) DF is a simple function of the pretransient (or initial) DF. The final DF is more "flattened" near a resonance when compared with the initial DF because of mixing due to the separatrix crossing of stellar orbits; this has important consequences for mode renewal, as discussed in Sections 5 and 6. The DF of a "scar" is defined as the difference between the final and initial DFs. It is localized around resonances and is the basic quantity required to calculate changes in all physical quantities. We derive an expression for the angular momentum absorbed from the transient by resonant stars.

The DFs of scars are calculated in Section 4 for a cool Mestel disk. This allows us to make quantitative estimates, guiding the rest of the paper. These DFs provide a phase-space picture of mass shifts across resonant surfaces, which determine the angular momentum absorbed from the transient, and the surface density profiles of scars. Simple expressions are derived for both quantities, together with numerical estimates. In Section 5, the results of the previous sections are gathered together to prove that the linear responses of the initial and final DFs are very different to a new perturbation with the same angular wavenumber and pattern speed as the original transient mode. The flattening of the DF inside resonant scars suppresses resonant torques in the final disk.

In Section 6, we address the problem of mode renewal in the final disk, by first showing that suppressed torques in the final disk also result in suppressed epicyclic heating. The suppression factor between the final and initial disks is small for linear modes with the same angular wavenumber and pattern speed as the transient. But it is likely to be of order unity for some other linear mode, the resonant curves of which do not lie within the scars of the final disk; these modes will, generically, have a different angular wavenumber or pattern speed. We propose a model of mode renewal and compare it with the simulations of SC14. Their physical insights regarding the growth, decay, and renewal of nonaxisymmetric modes generated by shot noise are interpreted in terms of our model, wherein scars act as sharp filters of a noisy generator, favoring the growth of linear modes with the lowest dissipation rates. We conclude in Section 7 with a brief consideration of the limitations and desirable extensions of our model of mode renewal, possible numerical tests, prospects for seeing them in the second *Gaia* data release, and speculation on the role of relic scars on the evolution of galactic disks.

2. Decay of Linear Modes

2.1. Disk Dynamics

The galactic disk consists of stars orbiting in a plane under the combined actions of their mutual self-gravity and external gravitational sources. Let (R, ϕ) be the polar coordinates of a star, and (p_R, p_ϕ) be the conjugate momenta; $p_R = \dot{R}$ is the radial velocity and $p_\phi = R^2 \dot{\phi}$ is the z-component of the orbital angular momentum per unit mass. We use $\Gamma = (p_R, p_\phi; R, \phi)$ to denote phase-space location and $d\Gamma = dp_R \, dp_\phi \, dR \, d\phi$ for phase volume. The mass of stars at time t in $d\Gamma$ is $f(\Gamma, t)d\Gamma$, where $f \geqslant 0$ is the mass DF with $\int d\Gamma f(\Gamma, t) =$ disk mass. The total gravitational potential acting on a star is

$$\Phi(R, \phi, t) = \Phi^{\text{disk}} + \Phi^{\text{halo}} + \Phi^{\text{ext}}, \quad (1a)$$

$$\Phi^{\text{disk}}(R, \phi, t) = -G \int d\Gamma' \frac{f(\Gamma', t)}{|\boldsymbol{R} - \boldsymbol{R}'|}, \quad (1b)$$

is the mean self-gravitational potential due to disk stars, where $\boldsymbol{R} = (R, \phi)$ and $\boldsymbol{R}' = (R', \phi')$ are position vectors in the disk plane. $\Phi^{\text{halo}}(R)$ is the potential of a dark halo in the disk plane, and $\Phi^{\text{ext}}(R, \phi, t)$ is a given external perturbation. The Hamiltonian governing the dynamics of a star is the energy per unit mass,

$$\mathcal{H}(\Gamma, t) = \frac{p_R^2}{2} + \frac{p_\phi^2}{2R^2} + \Phi(R, \phi, t). \quad (2)$$

The time evolution of the DF is governed by the collisionless Boltzmann equation (CBE):

$$\frac{df}{dt} \equiv \frac{\partial f}{\partial t} + [f, \mathcal{H}] = 0, \quad \text{where} \quad (3a)$$

$$[f, g] = \frac{\partial f}{\partial R}\frac{\partial g}{\partial p_R} - \frac{\partial f}{\partial p_R}\frac{\partial g}{\partial R} + \frac{\partial f}{\partial \phi}\frac{\partial g}{\partial p_\phi} - \frac{\partial f}{\partial p_\phi}\frac{\partial g}{\partial \phi} \quad (3b)$$

is the Poisson Bracket. Equations (1)–(3) determine the self-consistent evolution of the DF.

The unperturbed galactic disk is assumed to be stationary and axisymmetric, with Hamiltonian

$$\mathcal{H}_0(R, p_R, p_\phi) = \frac{p_R^2}{2} + \frac{p_\phi^2}{2R^2} + \Phi_0(R), \quad (4)$$

where $\Phi_0(R) = \Phi_0^{\text{disk}}(R) + \Phi^{\text{halo}}(R)$. Both $\mathcal{H}_0 = E$ and $p_\phi = L_z$ are constant along a stellar orbit. The radial and angular frequencies of the orbit are functions of (E, L_z) and are generally incommensurate. So, a generic orbit describes a "rosette," as it goes through many periapse and apoapse passages, eventually filling an annular disk between the pericenter radius $b_1(E, L_z)$ and the apocenter radius $b_2(E, L_z)$. Because the unperturbed DF is time independent, Equation (3) and the Jeans theorem imply that it must be of the form $f_0(E, L_z)$. Let $f_1(\Gamma, t)$ be a small perturbation to f_0. In the limit of an infinitesimal perturbation, f_1 satisfies the linearized CBE (LCBE):

$$\frac{\partial f_1}{\partial t} + [f_1, \mathcal{H}_0] + [f_0, \Phi_1] = 0, \quad (5)$$

where $\Phi_1(R, \phi, t) = \Phi_1^{\text{disk}} + \Phi^{\text{ext}}$ is the total potential perturbation.

2.2. Linear Modes

We are interested in nonaxisymmetric modal perturbations of the form

$$\Phi_1(R, \phi, t) = \varepsilon_p \exp(\gamma t)\Phi_a(R, \phi - \Omega_p t), \quad (6a)$$

$$f_1(\Gamma, t) = \varepsilon_p \exp(\gamma t)f_a(p_R, p_\phi, R, \phi - \Omega_p t). \quad (6b)$$

Here, $0 < \varepsilon_p \ll 1$ is a small parameter, Ω_p is a constant pattern speed, and $\gamma > 0$ for a perturbation that is applied gradually in time; γ can be taken to zero at the end of the calculation.

Following Kalnajs (1971), we introduce the action-angle variables, $(J_R, J_\phi; \theta_R, \theta_\phi)$, to study perturbations. The momenta are $(J_R, J_\phi = L_z)$, where $J_R = (1/\pi)\int_{b_1}^{b_2} dR \sqrt{2(E - \Phi_0(R) - L_z^2/2R^2)}$ is the radial action. J_R is a measure of the departure from a circular orbit: $J_R = 0$ for a circular orbit, and the amplitude of radial excursions increases with increasing J_R for given L_z. The conjugate coordinates are (θ_R, θ_ϕ), the radial and angular phases. The Hamiltonian governing the unperturbed time evolution of the action-angle variables is $E(J_R, L_z)$, the orbital energy per unit mass. This implies that J_R and L_z are constant along an orbit (which is expected), whereas their conjugate angles advance uniformly with time at the rates

$$\dot\theta_R = \Omega_R = \frac{\partial E}{\partial J_R} > 0, \qquad \dot\theta_\phi = \Omega_\phi = \frac{\partial E}{\partial L_z}. \quad (7)$$

We rewrite the unperturbed DF as $f_0(E, L_z) = F_0(J_R, L_z)$ and expand the mode functions of Equation (6) as Fourier series in the angles:

$$\Phi_a = \sum_{\ell,m} \widetilde\Phi_{\ell m} \exp\{i(\ell\theta_R + m(\theta_\phi - \Omega_p t))\}, \quad (8a)$$

$$f_a = \sum_{\ell,m} \widetilde F_{\ell m} \exp\{i(\ell\theta_R + m(\theta_\phi - \Omega_p t))\}, \quad (8b)$$

where the Fourier coefficients, $\widetilde\Phi_{\ell m} = (\widetilde\Phi_{-\ell,-m})^*$ and $\widetilde F_{\ell m} = (\widetilde F_{-\ell,-m})^*$, are functions of (J_R, L_z), and the sums are over all integer pairs (ℓ, m).

Using Equations (6) and (8) in the LCBE, we obtain the linear response as

$$\widetilde F_{\ell m}(J_R, L_z) = \left(\ell\frac{\partial F_0}{\partial J_R} + m\frac{\partial F_0}{\partial L_z}\right)\frac{i\widetilde\Phi_{\ell m}(J_R, L_z)}{\gamma + i\omega}, \quad (9)$$

where $\omega = \{\ell\Omega_R + m(\Omega_\phi - \Omega_p)\}$. A stationary DF corresponds to a marginally growing mode, obtained in the limit $\gamma \to 0_+$:

$$\widetilde F_{\ell m} \to \left(\ell\frac{\partial F_0}{\partial J_R} + m\frac{\partial F_0}{\partial L_z}\right)\left\{\frac{1}{\omega} + i\pi\delta(\omega)\right\}\widetilde\Phi_{\ell m}, \quad (10)$$

where $\delta(\ )$ is the Dirac delta function. Both terms within the { } are singular at resonances in action space, where

$$\omega = \ell\Omega_R(J_R, L_z) + m\{\Omega_\phi(J_R, L_z) - \Omega_p\} = 0. \quad (11)$$

For a given Ω_p, an (ℓ, m) resonance is a curve in action space. Away from the resonance, the response of Equation (10) is nonsingular and the δ-function does not contribute; mode structure may be studied by solving integral equations (see,

e.g., Kalnajs 1971; Evans & Read 1998). For a tightly wound spiral density wave, the self-consistent problem becomes "local" and can be solved to obtain the well-known Lin–Shu–Kalnajs dispersion relationship (Lin & Shu 1966; Kalnajs 1965); see Binney (2013) for a nice derivation.

2.3. Angular Momentum Budget

The δ-function part of the response of Equation (10) can be thought of as a "van Kampen" mode (see, e.g., Binney & Tremaine 2008). But it is a particular type of van Kampen mode and plays a fundamental role in determining angular momentum exchanges between the mode and resonant stars (Lynden-Bell & Kalnajs 1972). The total torque exerted by the mode on disk stars,

$$\mathcal{T} = -\int d\Gamma \frac{\partial\Phi_1}{\partial\phi}\{f_0 + f_1\} = -\int d\Gamma \frac{\partial\Phi_1}{\partial\phi}f_1, \quad (12)$$

is second order in the perturbation. Because the Poisson Bracket is invariant under canonical transformations, $\partial\Phi_1/\partial\phi = [\Phi_1, p_\phi] = [\Phi_1, L_z]$. Using Equations (6), (8), and (10) in Equation (12)—see Section 2.4 of Kaur & Sridhar (2018) for a simple derivation in the context of an unperturbed spherical galaxy—we obtain the Lynden-Bell & Kalnajs (LBK) torque formula:

$$\mathcal{T} = \sum_{\ell=-\infty}^{\infty}\sum_{m=1}^{\infty}\mathcal{T}_{\ell m}, \quad \text{where} \quad (13a)$$

$$\mathcal{T}_{\ell m} = -8\pi^3\varepsilon_p^2 m \int dJ_R dL_z \left(\ell\frac{\partial F_0}{\partial J_R} + m\frac{\partial F_0}{\partial L_z}\right)$$
$$\times \delta(\ell\Omega_R + m\{\Omega_\phi - \Omega_p\})|\widetilde\Phi_{\ell m}(J_R, L_z)|^2. \quad (13b)$$

The $\ell < 0$ and $\ell > 0$ resonances are the ILR and OLR, respectively; the principal ones are the ILR ($\ell = -1$) and the OLR ($\ell = 1$), and $\ell = 0$ is the CR.

For the mode to be stationary, every $\mathcal{T}_{\ell m} = 0$; for, if any $\mathcal{T}_{\ell m} \neq 0$, the exchange of angular momentum with resonant stars will make the perturbation time dependent. Indeed, $\mathcal{T}_{\ell m} \neq 0$ as Lynden-Bell & Kalnajs (1972) demonstrated for "epicyclic" disks, which are reasonable first approximations to cool galactic disks in which radial speeds are much smaller than circular speeds. An epicyclic DF, $F_0(J_R, L_z)$, has $(\partial F_0/\partial J_R) < 0$ and $|\partial F_0/\partial J_R| \gg |\partial F_0/\partial L_z|$. Then, $(\ell\,\partial F_0/\partial J_R + m\,\partial F_0/\partial L_z) \simeq \ell\,\partial F_0/\partial J_R$ at all Lindblad resonances, and $= m\partial F_0/\partial L_z$ at the CR. Using this in Equation 13(b), we can conclude:

a. $\mathcal{T}_{\ell m} < 0$ at all ILR, and $\mathcal{T}_{\ell m} > 0$ at all OLR.[1]

b. At the CR, the sign of $\mathcal{T}_{0m}$ is opposite to that of $\partial F_0/\partial L_z$, so the angular momentum exchange can be of either sign.

If, instead of a marginally growing mode, one considered a growing mode with $\gamma > 0$, then the δ-function in Equation 13(b) would be replaced by a Lorentzian function of width γ. For γ not too large, the signs of the $\mathcal{T}_{\ell m}$ would not change. Hence, we may expect the conclusions of items (a) and (b) to be still valid. Moreover, the process is accompanied by the excitation of epicyclic motions at all Lindblad resonances

---

[1] In the complementary local approach, angular momentum is transported by wave packets traversing the regions between the resonances, where the radial flux of angular momentum is the sum of gravitational and advective ("lorry transport") fluxes. The wave angular density is negative/positive inside/outside corotation (Binney & Tremaine 2008, Section 6.2.6).

(see footnote 2). Therefore, we expect nonaxisymmetric linear modes of a smooth DF $F_0(J_R, L_z)$ to be generically transient.

3. Resonant Deformation Due to an Adiabatic Transient

What changes does an axisymmetric DF $F_0(J_R, L_z)$ suffer due to a transient, nonaxisymmetric mode? Carlberg & Sellwood (1985) calculated the changes to $O(\varepsilon_p^2)$ for a transient spiral mode whose amplitude grew as $\exp(\gamma_1 t)$ for $t \leqslant 0$ and decayed as $\exp(-\gamma_2 t)$ for $t > 0$. In the limit of slow growth and decay, $\gamma_1, \gamma_2 \to 0_+$, the DF shows no lasting changes anywhere in phase space, except at the resonances where the linear response is singular. The singularities can be resolved only through an intrinsically nonlinear treatment of the CBE of Equation (3). We calculate the finite changes in the DF near a resonance, using the nonlinear theory of adiabatic capture into resonance (ST96).

When there is not much overlap of resonances—which is indeed true for a cool Mestel disk; see Section 4.2.1 and Figure 3—the dynamics near a resonance can be reduced to the standard pendulum form (Chirikov 1979; Monari et al. 2017), whose derivation is given in Section 3.1. In Section 3.2, we use the results of ST96 to determine the posttransient (or final) DF, which has the simple form given in Equation (27). The final DF is finite and differs from the initial DF only inside a region of width $O(\sqrt{\varepsilon_p})$ around a resonance. The changes in the disk are concentrated around resonances, which may be thought of as resonant scars left behind in phase space by the transient. In Section 3.3, we define the DF of a scar, which is the basic physical quantity required for calculating changes in disk properties. Equation (30) for the DF of a scar shows that it varies by $O(\sqrt{\varepsilon_p})$ over a region of width $O(\sqrt{\varepsilon_p})$ in action space. We derive an expression for the angular momentum exchanged between the transient mode and resonant stars. In contrast to the $O(\varepsilon_p^2)$ change of the linear theory (see Section 2.3), the change in the angular momentum within the scar is $O(\varepsilon_p^{3/2})$, which is larger. The global change in disk properties is explored for a cool Mestel disk in Sections 4 and 5.

3.1. Resonant Dynamics

The unperturbed orbits of stars in action-angle space are governed by the Hamiltonian, $E(J_R, L_z)$, with orbital frequencies, $\Omega_R(J_R, L_z)$ and $\Omega_\phi(J_R, L_z)$, given by Equation (7). The orbits are perturbed by a transient, adiabatically time-varying, nonaxisymmetric mode with a fixed angular wavenumber $m > 0$ and pattern speed Ω_p. The gravitational potential perturbation of the transient is

$$\Phi_{tr} = \varepsilon_p A(\varepsilon t) \Phi_a(R) \cos\{m(\phi - \Omega_p t) + \chi_a(R)\}. \quad (14)$$

Here, $0 < \varepsilon_p \ll 1$ is a small, but not infinitesimal, measure of the perturbation strength; $A(\varepsilon t) \geqslant 0$ is a dimensionless $O(1)$ time profile function, where $0 < \varepsilon \ll 1$ is the ratio of the orbital periods of stars to the timescales over which A varies;

---

and $\Phi_a(R)$ and $\chi_a(R)$ are the radial profile and phase functions, respectively.

Φ_{tr} can be rewritten in terms of the action-angle variables, $(J_R, L_z; \theta_R, \theta_\phi)$, as

$$\Phi_{tr} = \varepsilon_p A(\varepsilon t) \sum_{\ell=-\infty}^{\infty} [\widetilde{\Phi}_{\ell m} \exp\{i[\ell\theta_R + m(\theta_\phi - \Omega_p t)]\} + \text{complex conjugate}]. \quad (15)$$

Here, $\widetilde{\Phi}_{\ell m}(J_R, L_z)$ are complex Fourier coefficients that can be calculated from $\Phi_a(R)$ and $\chi_a(R)$. The perturbed orbits of stars are governed by the total Hamiltonian

$$H_{tot} = E(J_R, L_z) + \Phi_{tr}(J_R, L_z, \theta_R, \theta_\phi, t). \quad (16)$$

Resonances occur on curves in the (J_R, L_z) plane, on which Equation (11) is satisfied. We assume that the resonant curves for different ℓ, for the given $m > 0$, are well separated. For dynamics near some chosen (ℓ, m) resonant curve, the dominant contribution to Φ_{tr} comes from the term $[\widetilde{\Phi}_{\ell m} \exp\{i(\ell\theta_R + m(\theta_\phi - \Omega_p t) + \text{c.c.}]$.

The resulting resonant dynamics is conveniently described in terms of new canonical variables, which rotate with the perturbation at its pattern speed Ω_p. These are the "fast" and "slow" actions and angles, $(J_f, J_s; \theta_f, \theta_s)$:

$$J_f = J_R - (\ell/m)L_z, \qquad J_s = L_z/m; \quad (17a)$$

$$\theta_f = \theta_R, \qquad \theta_s = \ell\theta_R + m(\theta_\phi - \Omega_p t). \quad (17b)$$

In the corotating frame, every orbit acquires an extra regression of θ_s at the rate $m\Omega_p$, so the unperturbed dynamics is described by the (Jacobi) Hamiltonian

$$H_{r0}(J_f, J_s) = E(J_f + \ell J_s, mJ_s) - m\Omega_p J_s. \quad (18)$$

The fast angle advances at the $O(1)$ rate, $\dot{\theta}_f = \Omega_f = (\partial H_{r0}/\partial J_f) = \Omega_R > 0$. The slow angle varies at the rate $\dot{\theta}_s = \Omega_s$, where the slow frequency is

$$\Omega_s(J_f, J_s) = \frac{\partial H_{r0}}{\partial J_s} = \ell\Omega_R + m(\Omega_\phi - \Omega_p). \quad (19)$$

The resonance condition of Equation (11) is identical to $\Omega_s(J_f, J_s) = 0$, so Ω_s is small near the resonance. Solving this, we can obtain the equation of the resonant (ℓ, m) curve in the (J_f, J_s) plane as

$$J_s = J_*(J_f), \quad \text{where } \Omega_s(J_f, J_*(J_f)) = 0. \quad (20)$$

For galactic disks, we generally consider $J_* > 0$.

The Hamiltonian governing dynamics near $J_*(J_f)$ is obtained by adding the potential perturbation, $[\widetilde{\Phi}_{\ell m} \exp(i\theta_s) + \text{c.c.}]$, to the H_{r0} of Equation (18). We write $\widetilde{\Phi}_{\ell m} = -(1/2)\Phi_p \exp(-i\xi)$, where $\Phi_p(J_f, J_s)$ and $\xi(J_f, J_s)$ are real $O(1)$ functions. Then, the resonant Hamiltonian is

$$H_r = H_{r0}(J_f, J_s) - \varepsilon_p A(\varepsilon t)\Phi_p \cos(\theta_s - \xi). \quad (21)$$

Because H_r is independent of θ_f, $J_f = $ constant even though H_r is time dependent.[2] Resonant dynamics has been reduced to that of a system with 1.5 degrees of freedom, where (J_s, θ_s) dynamics is governed by H_r, in which J_f is treated as a constant parameter. Once $J_s(t)$ and $\theta_s(t)$ have been solved for, $\theta_f(t)$ can be determined by integrating $\dot{\theta}_f = \partial H_r/\partial J_f$.

H_r can be simplified further by expanding it in a Taylor series in J_s about $J_*(J_f)$. The first term, $H_{r0}(J_f, J_*)$, can be
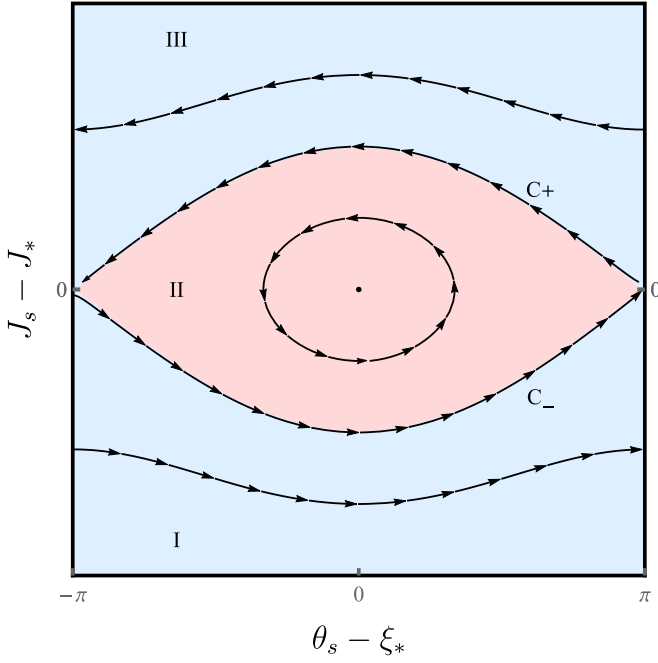
---

2 The constancy of the fast action implies that changes in J_R and L_z at the (ℓ, m) resonance are related to each other: $\delta J_R = (\ell/m)\delta L_z$ (Sellwood & Binney 2002). For smooth epicyclic DFs, items (a) and (b) of Section 2.2 imply that δL_z and ℓ have the same sign, so $\delta J_R > 0$ at all Lindblad resonances, and $\delta J_R = 0$ at the CR. Then, the change in the epicyclic energy (per unit mass), $\simeq \Omega_R \delta J_R$, is positive at all Lindblad resonances and very small at the CR. Thus, the disk heats up.

Figure 1. Phase space of the τ-frozen Hamiltonian. Orbits follow the isocontours of H of Equation (22), as indicated by the arrows. Trapped orbits are in region II (red), and circulating orbits are in regions I and III (blue).

dropped because it does not contribute to the dynamics of (J_s, θ_s). Because $(\partial H_{r0}/\partial J_s)_{J_s=J_*} = \Omega_s(J_s, J_*) = 0$, the linear term in $(J_s - J_*)$ is absent. Then, the unperturbed Hamiltonian $H_{r0}(J_f, J_s) \to (1/2)B_*(J_s - J_*)^2$, where $B_*(J_f) = (\partial^2 H_{r0}/\partial J_s^2)_{J_s=J_*} = (\partial \Omega_s/\partial J_s)_{J_s=J_*}$. We can also set $J_s = J_*$ in the perturbation: $\Phi_p(J_f, J_s) \to \Phi_*(J_f) = \Phi_p(J_f, J_*)$ and $\xi(J_f, J_s) \to \xi_*(J_f) = \xi(J_f, J_*)$. Then, the resonant Hamiltonian governing (J_s, θ_s) dynamics reduces to the standard pendulum form:

$$H = \frac{1}{2}B_*(J_s - J_*)^2 - \varepsilon_p A(\varepsilon t)\Phi_* \cos(\theta_s - \xi_*). \quad (22)$$

There are two small parameters in the problem: the nonlinearity of the perturbation, ε_p, and the adiabaticity parameter, ε. Both are infinitesimal for the linear theory of quasi-steady perturbations discussed in Section 2. Our goal is to take the next step of dealing directly with the lowest-order nonlinear effects of a small, but not infinitesimal, ε_p. In this section, we solve the problem for the adiabatic ordering, $\varepsilon \ll \varepsilon_p$, the likely consequences of relaxing which are discussed briefly in Section 7. The adiabatic dynamics of H is controlled by the time-varying A, which is conveniently kept track of by the "slow" time variable $\tau = \varepsilon t$, so we write $A(\tau)$.

Figure 1 shows the phase flow of the "τ-frozen" H of Equation (22) in (J_s, θ_s) space for some $A(\tau) \neq 0$.[3] In this limit, H is a constant of motion, so orbits follow its isocontours. The phase ξ_* can always be chosen (by shifting by π, if necessary) such that Φ_* has the same sign as B_*. Then, the elliptic fixed point is at (J_*, ξ_*), about which the entire Hamiltonian flow is reflection-symmetric in (J_s, θ_s) space. B_* can be of either sign; we chose $B_* < 0$ to represent the flow in Figure 1, because this is the case for the Mestel disk in the epicyclic limit—see

---

[3] From Equation (17), we note that, as θ_R and θ_ϕ increase by 2π, θ_f increases by 2π whereas θ_s increases by $2m\pi$. So there are m islands of which only one is shown in Figure 1.

Equation (44).[4] The upper and lower separatrices, $\mathcal{C}_+$ and $\mathcal{C}_-$, are the two solutions of $H = E_{sx}(\tau; J_f) = \varepsilon_p A(\tau)\Phi_* \leqslant 0$, given by

$$J_s = J_* \pm 2\sqrt{\frac{E_{sx}}{B_*}} \cos\{(\theta_s - \xi_*)/2\}. \quad (23)$$

$\mathcal{C}_\pm$ meet at the hyperbolic fixed point $(J_*, \xi_* \pm \pi)$ and divide the phase space into three different regions.

a. $H \leqslant E_{sx} \leqslant 0$ in regions I and III (blue regions in Figure 1), which have circulating orbits whose θ_s advance monotonically. $\mathcal{C}_\pm$ can be thought of as the limiting circulating orbits belonging to III and I, respectively. Because H is an even function of $(J_s - J_*)$, a given H corresponds to two orbits, one in I and the other in III, which is obtained by reflection about the elliptic fixed point.

b. $E_{sx} < H \leqslant -E_{sx}$ in region II (red region in Figure 1), which can be thought of as a resonant island. This consists of trapped orbits librating around the elliptic fixed point, where H takes its maximum value of $-E_{sx} \geqslant 0$.

c. In II, the libration frequency decreases as H decreases, from $\sqrt{B_* E_{sx}}$ at the elliptic fixed point for $H = -E_{sx}$, to zero as $H \to E_{sx}$. As H decreases further, we enter III and I where the circulation frequency is zero for $\mathcal{C}_\pm$ and increases in magnitude as H decreases further.

When the variation of $A(\tau)$ with τ is taken into account, H is no longer a conserved quantity. Because $\varepsilon \ll \varepsilon_p$, the motion is adiabatic in regions that are not in the immediate vicinity of $\mathcal{C}_\pm$. Then, the phase area, $\oint d\theta_s(J_s - J_*)$ enclosed by isocontours of H, is an adiabatic invariant. This is a function of (H, τ), which is discontinuous across $\mathcal{C}_\pm$, because the topology of orbits changes from trapped to circulating or vice versa. The fate of an orbit when it encounters a slowly moving separatrix is very sensitive to θ_s at encounter, and the phase area is no longer a conserved quantity. For instance, a circulating orbit could get captured by the resonant island or become another circulating orbit on the other side of the island; or a trapped orbit may escape from the resonant island through either of the separatrices. This process was described in probabilistic terms by Goldreich & Peale (1966) for single orbits in the context of solar system dynamics. ST96 applied this to stellar systems and derived the equations governing the time evolution of the DF. Below we apply ST96 to derive the final DF, in terms of the above initial DF, after the passage of an adiabatic transient.

3.2. Posttransient DF

For a transient mode, we assume that $A(\tau)$ in Equation (22) increases monotonically from zero at $\tau_<$, reaches a maximum value of unity at τ_0, and then decreases monotonically to zero at $\tau_>$. At $\tau = \tau_<$, when A is zero, the initial DF

$$F_{in}(J_f, J_s) = F_0(J_f + \ell J_s, mJ_s) \quad (24)$$

is given as a smooth function of (J_f, J_s). Here we derive the final DF after the passage of the transient.

As noted in the final paragraph of Section 3.1, adiabatic dynamics conserves the phase area, $\oint d\theta_s(J_s - J_*)$, of orbits

---

[4] Were B_* positive, the arrows in Figure 1 would be reversed, but there would be no change in the physics of the process discussed in this section.

that are away from $\mathcal{C}_{\pm}$. It is a function of (H, τ), with discontinuities across $\mathcal{C}_{\pm}$. ST96 uses the conservation and nonconservation of the phase area in a basic manner. Because H is an even function of $(J_s - J_*)$, so is the phase area. This means—see item (a) of Section 3.1—that a given value of the phase area refers to two different orbits, one in I and its reflection in III. But the initial DF of Equation (24) is, in general, not reflection-symmetric about $J_s = J_*$; see Equation (48) for the Mestel disk. So the phase area is not a good variable to use to follow the evolution of the DF. However, this is readily fixed by exploiting a certain latitude in the choice of the relative signs in the three regions. Accordingly, we define

$$
K = \begin{cases} (2\pi)^{-1} \oint d\theta_s (J_s - J_*) & \text{in region I,} \\ -(2\pi)^{-1} \oint d\theta_s (J_s - J_*) & \text{in regions II and III,} \end{cases} \tag{25}
$$

which is an adiabatic invariant for orbits away from $\mathcal{C}_{\pm}$. The integrals are taken over the τ-frozen orbits, $(J_s - J_*) = \pm\sqrt{2[H + \varepsilon_p A(\tau)\Phi_* \cos(\theta_s - \xi_*)]/B_*}$, as applicable. Unlike the phase area, K takes different values in I and III. Because $\dot{\theta}_s = B_*(J_s - J_*)$, we have $\oint d\theta_s (J_s - J_*) = B_* \oint dt (J_s - J_*)^2 \leqslant 0$. So $K \leqslant 0$ in I, and $K \geqslant 0$ in II and III: indeed, two orbits in I and III with the same (H, τ) have equal and opposite values of K. So, K is a good variable to use to describe the evolution of a general initial DF of Equation (24).[5]

ST96 provides the equations governing the adiabatic time evolution of the DF as a function of (J_f, K). These are used in Appendix A to derive Equation (27) for the final DF in seven simple steps. Below we give a brief account of the physics of this process.

The first step is to write the initial DF as a function of J_f and K. At the initial time $\tau_<$, when $A = 0$, the disk is axisymmetric with DF given by Equation (24). Both $\mathcal{C}_{\pm}$ collapse to the line $J_s = L_*$, so trapped orbits are absent. Because the measure of region II is zero, region I consists of orbits with $J_s \leqslant J_*$ and region III has orbits with $J_s \geqslant J_*$. Circulating orbits are governed by $H = (1/2)B_*(J_s - L_*)^2$. Then, $J_s = \text{constant}$ along orbits, so $(J_s - J_*)$ can be pulled out of the integral in Equation (25). Because $\dot{\theta}_s = B_*(J_s - J_*)$ is positive in I and negative in III, $\oint d\theta_s$ is equal to 2π in I and -2π in III. Hence, $K = J_s - J_*$, and the initial DF can be written as $F_{in}(J_f, J_* + K)$. Identical considerations apply at the final time $\tau_>$, when $A = 0$ again.

Between $\tau_<$ and $\tau_>$, the transient is nonzero. As $\mathcal{C}_{\pm}$ expand and contract symmetrically about the resonant line $J_s = J_*(J_f)$, the disk undergoes a sequence of adiabatic transformations through nonaxisymmetric states. But the final DF is axisymmetric, just like the initial DF. Orbits may be divided into two classes: those that never cross $\mathcal{C}_{\pm}$ and those that experience separatrix crossing. The dividing line between these two classes is given by the maximum excursions of $\mathcal{C}_{\pm}$ away from J_*, which happens at τ_0 when $A = 1$. At this time, the K

corresponding to $\mathcal{C}_{\pm}$ are equal to $\pm\Delta J(J_f)$, where

$$
\Delta J(J_f) = \frac{4}{\pi}\sqrt{\frac{\varepsilon_p \Phi_*(J_f)}{B_*(J_f)}} > 0 \tag{26}
$$

is derived in Equation (107).

1. Orbits with $|J_s - J_*| \geqslant \Delta J$ at the initial time never encounter $\mathcal{C}_{\pm}$. These remain circulating orbits for all time, and K is an adiabatic invariant. So, the DF maintains a frozen form when expressed as a function of (J_f, K). Because $K = J_s - J_*$ at the initial and final times, the final DF is equal to the initial DF.

2. Orbits with $|J_s - J_*| < \Delta J$ at the initial time experience separatrix crossing twice, first in the expansion phase and second in the contraction phase. Consider the circulating orbits with $K = K_1/2$ in region III and their reflected counterparts with $K = -K_1/2$ in region I, where K_1 can take any value between 0 and $2\Delta J$.

2a. Let τ_1 be the time between $\tau_<$ and τ_0 when the expanding $\mathcal{C}_{\pm}$ cross $\pm K_1/2$, respectively. The circulating orbits are now trapped by the expanding island and turned into librating orbits with $K = K_1$, just inside $\mathcal{C}_{\pm}$. Because the motions of the separatrices are reflection-symmetric, according to ST96, the DF of the newly formed librating orbits contains equal mixtures of the DFs of the circulating orbits at $\pm K_1/2$.

2b. Following this, $\mathcal{C}_{\pm}$ expand away from these librating orbits, attaining maximum expansion at τ_0, after which they contract. Meanwhile, the DF of the librating orbits at K_1 remains frozen until $\mathcal{C}_{\pm}$ encounter them during their contraction phase at the unique time τ_2 (which lies between τ_0 and $\tau_>$).

2c. As $\mathcal{C}_{\pm}$ cross them, the librating orbits are liberated from the shrinking island into circulating orbits with $K = \pm K_1/2$ in III and I, respectively. According to ST96, the DFs of these circulating orbits are equal to the DF of the librating orbits at K_1 just prior to the encounter.

2d. Further contraction of $\mathcal{C}_{\pm}$ leaves the DF of $\pm K_1/2$ unchanged until the final time $\tau_>$. Hence, the final DF at (J_f, J_s) is a mixture containing equal proportions of the initial DF at (J_f, J_s) and the initial DF at $(J_f, 2J_* - J_s)$.

Therefore, the final axisymmetric DF is

$$
F_{fin}(J_f, J_s) = \begin{cases} \dfrac{1}{2}\{F_{in}(J_f, J_s) + F_{in}(J_f, 2J_* - J_s)\} \\ \qquad\qquad\qquad \text{for } |J_s - J_*| < \Delta J, \\ F_{in}(J_f, J_s) \quad \text{otherwise.} \end{cases} \tag{27}
$$

As shown in Figure 2, the final DF is equal to the initial DF, except within a "scar" of half-width $\Delta J(J_f) \propto \sqrt{\varepsilon_p}$ straddling the resonant line. $F_{fin}(J_f, J_s)$ is discontinuous at the scar boundaries, $J_s = J_*(J_f) \pm \Delta J(J_f)$, because there is a sharp difference, in the adiabatic limit, between the dynamical histories of regions that have experienced separatrix crossing and those that have not. Within the scar, F_{fin} is an even function of $(J_s - J_*)$.

We can simplify Equation (27) by using the fact that $F_{in}(J_f, J_s)$ is a smooth function of J_s, and the scar occupies a narrow, $O(\sqrt{\varepsilon_p})$, region of phase space. So, for $|J_s - J_*| < \Delta J$, the DF can be expanded in a Taylor series about $J_s = J_*(J_f)$:

$$
F_{in}(J_f, J_s) = F_{in}^{(0)} + F_{in}^{(1)}(J_s - J_*) + \frac{1}{2}F_{in}^{(2)}(J_s - J_*)^2 + \dots,
$$

$$\tag{28}$$

---

[5] A similar choice is implicit in the ranges given in Equation (6) of ST96, but was not stated explicitly there.
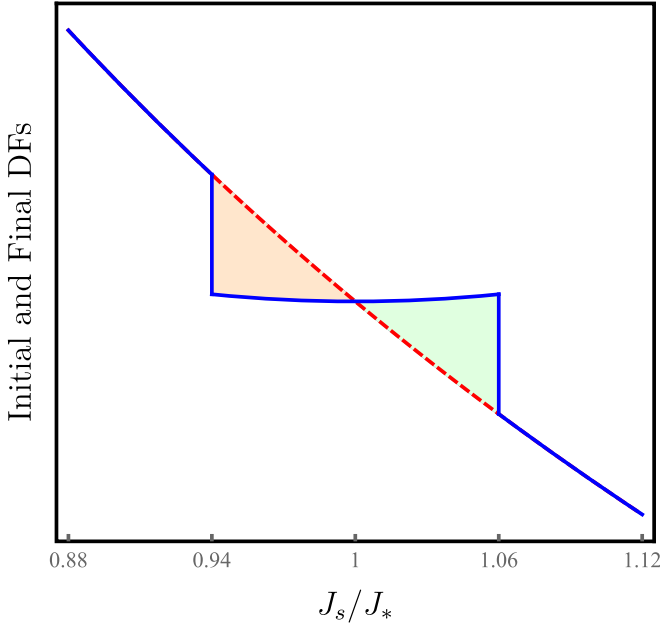
Figure 2. Initial and final DFs near a scar. The DFs are plotted as functions of J_s (in units of J_*) for some constant J_f. The dashed red curve is the initial DF, F_{in}, which is a smooth function of J_s. The solid blue curve shows the final DF, F_{fin} of Equation (27). $F_{fin} = F_{in}$ outside the scar of half-width $\Delta J = 0.02\, J_*$ and is flattened within the scar. The DF of the scar, ΔF of Equation (30), is indicated by the shaded regions, green for positive and red for negative. In this $J_f = $ constant slice, mass is transferred from left to right.

where $F_{in}^{(n)}(J_f) = (\partial^n F_{in}/\partial J_s^n)$ evaluated at $J_s = J_*(J_f)$ are $O(1)$ functions of J_f. Using this in Equation (27), we obtain

$$F_{fin}(J_f, J_s) = \begin{cases} F_{in}^{(0)} + \dfrac{1}{2}F_{in}^{(2)}(J_s - J_*)^2 + \ldots \\ \qquad\qquad \text{for } |J_s - J_*| < \Delta J, \\ F_{in}(J_f, J_s) \quad \text{otherwise.} \end{cases} \quad (29)$$

Within the scar, the final DF is a sum over the even terms of Equation (28). Comparing Equation (28) with Equation (29), we see that, well within the scarred region, F_{in} is a linear function of $(J_s - J_*)$, whereas F_{fin} is a quadratic function of $(J_s - J_*)$. Close to the resonance, the final DF is a more flattened function of J_s (on any $J_f = $ constant surface) than the initial DF; see Figure 2. This flattening is analogous to the resonant flattening of the velocity space DF in the Landau damping of plasma waves.

3.3. DF of a Scar

Because the final DF differs from the initial DF only within a narrow strip around the resonant line, it is useful to isolate these changes by defining the DF of a scar as the difference between the final and initial DFs:

$$\Delta F(J_f, J_s) = F_{fin}(J_f, J_s) - F_{in}(J_f, J_s)$$

$$= \begin{cases} \dfrac{1}{2}\{F_{in}(J_f, 2J_* - J_s) - F_{in}(J_f, J_s)\} \\ \qquad\qquad \text{for } |J_s - J_*| < \Delta J, \\ 0 \qquad\qquad \text{otherwise.} \end{cases} \quad (30)$$

This is indicated in Figure 2 by the shaded regions between the final and initial DFs. Within the scar, ΔF is an odd function of

$(J_s - J_*)$ and discontinuous at the scar boundaries. Because $\int dJ_s\, \Delta F(J_f, J_s) = 0$, the total mass in the scar is zero. At each value of J_f, mass has been shifted across the resonance. In the example shown in Figure 2, ΔF is positive for $J_s > J_*$ and negative for $J_s < J_*$.

The DF of a scar is the basic quantity required to calculate changes in the physical properties of the disk. ΔF is used in Section 3.3.1 to derive a formula for the angular momentum absorbed from the transient mode by resonant stars. Below we describe some general features of the geometry of a scarred region in the (J_f, J_s) plane and then simplify the expression for ΔF.

a. We can simplify Equation (30) by using the Taylor series expansion of Equation (28). Then,

$$\Delta F(J_f, J_s) = \begin{cases} -F_{in}^{(1)}(J_s - J_*) - \dfrac{1}{6}F_{in}^{(3)}(J_s - J_*)^3 - \ldots \\ \qquad\qquad \text{for } |J_s - J_*| < \Delta J, \\ 0 \qquad\qquad \text{otherwise.} \end{cases} \quad (31)$$

Within the scar, ΔF is equal to (-1) times the sum of the odd terms of Equation (28). The first term is $O(\sqrt{\varepsilon_p})$, whereas the second term is $O(\varepsilon_p^{3/2})$, which is much smaller. Hence ΔF has $O(\sqrt{\varepsilon_p})$ variations across the scar of width $\propto \sqrt{\varepsilon_p}$. Therefore, a good measure of the nonlinearity of the problem is given by the ratio

$$\frac{\Delta J}{J_*} = \frac{4}{\pi}\sqrt{\frac{\varepsilon_p \Phi_*}{B_* J_*^2}} \sim O(\sqrt{\varepsilon_p}) \ll 1. \quad (32)$$

From Equation (31), we can also infer that the direction of the shift of mass across the resonance depends mainly on the sign of $F_{in}^{(1)}(J_f)$. Generally, for $F_{in}^{(1)} \gtrless 0$, mass has been shifted from $(J_s \gtrless J_*)$ to $(J_s \lessgtr J_*)$.

b. The extent of the scar along J_f can be determined as follows: because $J_R \geqslant 0$, Equation (17) implies that $J_f \geqslant -\ell J_s$. Then, $J_f \geqslant j_0$, where j_0 is the value of J_f where the resonant line $J_s = J_*(J_f)$ intersects the lower boundary $J_f = -\ell J_s$. Hence, the minimum value of J_f satisfies the equation

$$j_0 = -\ell J_*(j_0). \quad (33)$$

For the CR, $j_0 = 0$ because $\ell = 0$. For the Lindblad resonances, $\ell \neq 0$, and this equation must be solved to get j_0. Because J_* is usually positive for galactic disks, $j_0 > 0$ for the inner Lindblad resonances (which have $\ell < 0$) and $j_0 < 0$ for the outer Lindblad resonances (which have $\ell > 0$).

c. The half-width of the scar $\Delta J(J_f)$ is determined by the radial profile of the transient mode and can assume varied forms depending on whether the perturbation is spiral or bar like. The functional form must be either calculated from a model of observational data or taken from numerical simulations. One general property we can infer directly is that it must vanish at the lower limit of J_f, i.e., $\Delta J(J_f) \to 0$ as $J_f \to j_0$, at all Lindblad resonances.[6]

---

[6] This can be understood as follows. At $J_f = j_0$, the allowed values of J_s are one-sided about the resonant value, $J_*(j_0) = -j_0/\ell > 0$; for the inner Lindblad resonances, $J_s \leqslant J_*(j_0)$, and for the outer Lindblad resonances, $J_s \geqslant J_*(j_0)$. But, for the pendulum Hamiltonian of Equation (22), the allowed deviations of J_s must necessarily be symmetric about $J_*(j_0)$. This is possible only when both $\mathcal{C}_\pm$ collapse to the line $J_s = J_*(j_0)$, when the resonant island has zero area. Therefore, $\Delta J(j_0) = 0$ at all Lindblad resonances. We saw in item (b) above that $j_0 = 0$ for the CR, so symmetrical deviations of J_s about $J_*(j_0 = 0)$ are indeed allowed, and $\Delta J(j_0 = 0)$ need not vanish at the CR.

3.3.1. Angular Momentum Exchange

The transfer of mass across the resonant line leads to a change in the angular momentum of stars in the scarred region. The angular momentum absorbed by the resonant stars from the transient mode is

$$\mathcal{L}_{\mathrm{abs}} = 4\pi^2 m \int_{j_0}^{\infty} dJ_{\mathrm{f}} \int dJ_{\mathrm{s}} \Delta F(J_{\mathrm{f}}, J_{\mathrm{s}}) m J_{\mathrm{s}}$$
$$= 4\pi^2 m^2 \int_{j_0}^{\infty} dJ_{\mathrm{f}} \int dJ_{\mathrm{s}} \Delta F(J_{\mathrm{f}}, J_{\mathrm{s}})(J_{\mathrm{s}} - J_*), \quad (34)$$

where we have used $\int dJ_{\mathrm{s}} \Delta F(J_{\mathrm{f}}, J_{\mathrm{s}}) = 0$. Using Equation (31), we obtain

$$\mathcal{L}_{\mathrm{abs}} \simeq -\frac{8\pi^2}{3} m^2 \int_{j_0}^{\infty} dJ_{\mathrm{f}} \; F_{\mathrm{in}}^{(1)}(J_{\mathrm{f}})[\Delta J(J_{\mathrm{f}})]^3. \quad (35)$$

This shows that $\mathcal{L}_{\mathrm{abs}}$ is generically $O(\varepsilon_{\mathrm{p}}^{3/2})$, which is somewhat larger than the $O(\varepsilon_{\mathrm{p}}^2)$ change of the linear theory discussed in Section 2.3. The sign of $\mathcal{L}_{\mathrm{abs}}$ can be positive or negative. This is computed in Section 4.3, where it will become clear how differently physical quantities behave at the three kinds of resonances, namely the inner and outer Lindblad resonances and the CR.

4. Scars in a Cool Mestel Disk

Equations (30) and (31) are compact expressions for ΔF, the DF of the axisymmetric scar left behind by the passage of a transient, adiabatic, nonaxisymmetric mode. But these hide the important dependence of the sense of mass shifts across resonances—hence the signs of the resonant angular momentum exchanges, $\mathcal{L}_{\mathrm{abs}}$ of Equation (35)—on the integers (ℓ, $m > 0$) labeling different resonances. Only when this is revealed would we have a physical picture of the interactions of the transient nonaxisymmetric mode with stars at the inner/ outer Lindblad and CRs.

In this section, we make explicit the general results of Section 3 and compute physical quantities for a cool Mestel disk, a model that has been used extensively in analytical and numerical work. Some properties of a cool Mestel disk are summarized in Section 4.1; see Binney & Tremaine (2008) and references therein for more details. The effect of the transient mode on the disk is considered in Section 4.2, where we compute resonance locations and scar widths. The principal resonances, ILR ($\ell = -1$), the CR ($\ell = 0$), and the OLR ($\ell = +1$), are well separated in phase space. In Section 4.3, we compute $\mathcal{L}_{\mathrm{abs}}$ and discuss its properties as a function of (ℓ, m), paying attention to the principal resonances.

The rearrangement of mass in phase space is best appreciated by plotting ΔF in the (J_R, L_z) plane. This is because (J_{f}, J_{s}) are useful only in the neighborhood of resonances, whereas (J_R, L_z) are global coordinates; we always have $J_R \geqslant 0$, and $L_z > 0$ for a disk of prograde stars. In Section 4.4, we discuss the properties of ΔF in the (J_R, L_z) plane, and its direct implications for the mass shifts at the principal resonances. Descending from phase space to real space, ΔF induces an axisymmetric change, $\Delta\Sigma(R)$, in the disk surface density. This is computed in Section 4.4.2 and Appendix B.1, and found to be localized around resonant radii. The gravitational perturbation due to $\Delta\Sigma(R)$ is computed in Section 5 and used to showed that resonant torques in the scarred Mestel disk, due to a certain class of linear modes, are highly suppressed.

4.1. Unperturbed Disk

The exact DF for a Mestel disk, given in Toomre (1977) and Binney & Tremaine (2008), consists of stars orbiting only in a prograde sense, so $L_z > 0$. The surface density, $\Sigma_0(R) \propto 1/R$, gives rise to an attractive, radial gravitational force $\propto 1/R$, so the circular speed of a star is independent of R (i.e., a flat rotation curve). The disk is embedded in a static spherical halo with a three-dimensional mass density profile $\rho_{\mathrm{halo}}(r) \propto 1/r^2$, which exerts a radial force $\propto 1/r$. The total radial acceleration felt by a star, due to the disk and halo, in the disk plane can be written as $a_0(R) = -V_0^2/R$, where V_0 is the constant circular speed. We write $\Sigma_0(R) = \eta V_0^2/2\pi GR$, where $0 < \eta \leqslant 1$ is the fractional contribution of the disk to the total radial force. The radial velocity dispersion σ_0 is constant.

In a cool disk, $\sigma_0 \ll V_0$, and most of the stars are on near-circular orbits. The guiding-center radius of an orbit, $R_{\mathrm{g}}(L_z)$, is determined by solving $L_z^2 = -R^3 a_0(R)$, which gives $R_{\mathrm{g}}(L_z) = L_z/V_0$. The orbital and epicyclic frequencies are given by

$$\Omega_0(L_z) = \sqrt{-\left.\frac{a_0(R)}{R}\right|_{R=R_{\mathrm{g}}}} = \frac{V_0^2}{L_z}, \quad (36a)$$

$$\kappa_0(L_z) = \sqrt{-\left.\frac{1}{R^3}\frac{d}{dR}[R^3 a_0(R)]\right|_{R=R_{\mathrm{g}}}} = \sqrt{2}\,\frac{V_0^2}{L_z}. \quad (36b)$$

The typical epicyclic radius is $R_{\mathrm{epi}} = \sigma_0/\kappa_0 = 2^{-1/4}\beta^{-1/2} R_{\mathrm{g}}$, where $\beta = \sqrt{2}\,(V_0/\sigma_0)^2 \gg 1$ is a dimensionless measure of disk coolness. In the epicyclic limit, $R_{\mathrm{epi}} \ll R_{\mathrm{g}}$, the radial action is given by

$$J_R \simeq \frac{p_R^2}{2\kappa_0(L_z)} + \frac{\kappa_0(L_z)}{2}[R - R_{\mathrm{g}}(L_z)]^2 \geqslant 0. \quad (37)$$

The Schwarzschild DF for a cool Mestel disk is

$$F_0(J_R, L_z) = \frac{C}{L_z}\exp\left\{-\beta\frac{J_R}{L_z}\right\}, \qquad L_z > 0, \quad (38)$$

where $C = \eta\beta V_0/4\pi^2 G$ is a constant. At any given $L_z > 0$, most stars have $J_R/L_z < \beta^{-1} \ll 1$. Figure 3 shows some isocontours of F_0 in the (J_R, L_z) plane and the locations of the principal resonances.[7]

The epicyclic Hamiltonian governing the unperturbed stellar orbits is the sum of the energies (per unit mass) in circular and epicyclic motions:

$$E(J_R, L_z) = \frac{V_0^2}{2} + V_0^2\ln\left(\frac{L_z}{V_0 R_0}\right) + \kappa_0(L_z)J_R, \quad (39)$$

where R_0 is an arbitrary length scale. Then, the radial and angular frequencies are

$$\Omega_R = \frac{\partial E}{\partial J_R} = \kappa_0(L_z), \quad (40a)$$

$$\Omega_\phi = \frac{\partial E}{\partial L_z} = \Omega_0(L_z) - \kappa_0(L_z)\frac{J_R}{L_z} \simeq \Omega_0(L_z), \quad (40b)$$

---

[7] The loci of the resonances are straight lines of infinite slopes in the epicyclic limit we use. The resonant curves actually have finite slopes, but this does not affect our calculations because we calculate in the epicyclic limit, $J_R/L_z \ll 1$.
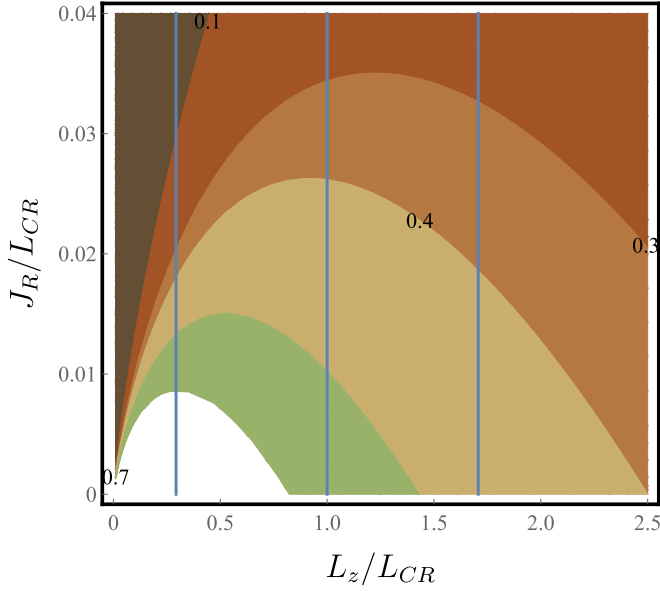
Figure 3. Cool Mestel DF in the (J_R, L_z) plane. Isocontours of $F_0(J_R, L_z)$ of Equation (38) in units of $C\Omega_p/V_0^2$, for $\beta = 35$. J_R and L_z are given in units of $L_{CR} = V_0^2/\Omega_p$. The three vertical blue lines, read left to right, mark the locations of the ILR, CR, and OLR for an $m = 2$ mode.

where the $O(J_R/L_z) < \beta^{-1} \ll 1$ term in Ω_ϕ is usually dropped in epicyclic theory.

4.1.1. Stability, Responsiveness, and Choice of Parameters

For the disk to be stable to axisymmetric perturbations, the Toomre parameter $Q = \sigma_0\kappa_0/3.36G\Sigma_0 > 1$. In a Mestel disk, $Q \simeq \pi/\eta\sqrt{\beta}$ is a constant independent of R. Because $\eta \leqslant 1$, we must have $Q\sqrt{\beta} \geqslant \pi$. Because $Q > 1$, this is always satisfied if $\beta \geqslant \pi^2 \simeq 10$. For fiducial values, $V_0 = 200\,\mathrm{km\,s}^{-1}$ and $\sigma_0 \lesssim 40\,\mathrm{km\,s}^{-1}$, we have $\beta \gtrsim 35$, so the disks we consider are indeed linearly stable to axisymmetric perturbations. Then the relative magnitude of the term that was dropped in Equation 40(b) is $O(J_R/L_z) < \beta^{-1} \lesssim 0.03$. The ratio of the typical epicyclic radius to the guiding-center radius is $R_{\rm epi}/R_{\rm g} \sim 2^{-1/4}\beta^{-1/2} \lesssim 0.14$. Whereas the unperturbed disk must necessarily be linearly stable, it must also be responsive to nonaxisymmetric perturbations. This implies that Q should not be too large; generally, $Q \lesssim 2$ for the disk to be responsive to swing amplification of nonaxisymmetric perturbations (Binney & Tremaine 2008, Section 6.3).

Aside from V_0, which sets the velocity scale, the natural parameters of the cool Mestel disk are the dimensionless quantities Q and β. This is because they can be simply and independently specified: $1 < Q < 2$ is tightly constrained by axisymmetric stability and responsiveness to nonaxisymmetric perturbations; we need only require $\beta \geqslant 10$, but we will use $\beta \gtrsim 35$, which is more relevant to galaxies like the Milky Way. In the calculations below, we use η and β, because the formulae appear simplest in these variables. When specific estimates are needed, we set $\eta \to \pi/Q\sqrt{\beta}$ and express quantities in terms of Q and β.

4.2. Perturbation due to a Transient Mode

The disk is perturbed by an m-armed, small-amplitude, adiabatic transient mode with pattern speed Ω_p, as discussed in the previous section. The potential perturbation is given by

Equations (14) and (15), and reproduced below:

$$\Phi_{\rm tr} = \varepsilon_p A(\varepsilon t)\Phi_a(R)\cos\{m(\phi - \Omega_p t) + \chi_a(R)\}$$

$$= \varepsilon_p A(\varepsilon t) \sum_{\ell=-\infty}^{\infty} [\widetilde{\Phi}_{\ell m}\exp\{i[\ell\theta_R + m(\theta_\phi - \Omega_p t)]\}$$

$$+ \text{complex conjugate}].$$

The transient leaves in its wake scars at different (ℓ, m) resonances spread across the disk. Here we compute resonance locations and scar widths.

4.2.1. Resonance Locations and Unperturbed Frequencies

Using the epicyclic frequencies of Equations 40(a) and (b) in Equation (11), we obtain the resonance condition

$$\ell\kappa_0(L_z) + m\{\Omega_0(L_z) - \Omega_p\} = 0. \tag{41}$$

Solving this, the resonant line in the (J_R, L_z) plane is $L_z = L_* = (V_0^2/\Omega_p)[1 + \sqrt{2}\,(\ell/m)]$, which is independent of J_R. Because the Mestel DF consists of stars with positive orbital angular momenta, the resonance exists only when $L_* > 0$; henceforth we assume that $(\ell, m > 0)$ are such that $[1 + \sqrt{2}\,(\ell/m)] > 0$.[8]

We can introduce the fast and slow action-angle variables of Equation (17) in the vicinity of the resonant lines, $L_z = L_*$, in the (J_R, L_z) plane. In the $(J_{\rm f}, J_{\rm s})$ plane, the equation for the resonant line is $J_{\rm s} = J_*$, where

$$J_* = \frac{L_*}{m} = \frac{V_0^2}{m\Omega_p}\left[1 + \sqrt{2}\,\frac{\ell}{m}\right] \tag{42}$$

is independent of $J_{\rm f}$. The principal resonances ($\ell = -1, 0, +1$) are indeed well separated in action space (see Figure 3), as was assumed in the derivation of the pendulum Hamiltonian in Section 3.1. The fast and slow frequencies can be calculated from Equations 40(a) and (b). $\Omega_{\rm f}(J_{\rm s}) = \Omega_R = \sqrt{2}\,V_0^2/mJ_{\rm s} \sim O(1)$ and

$$\Omega_{\rm s}(J_{\rm s}) = \ell\Omega_R + m\Omega_\phi - m\Omega_p \simeq m\Omega_p\left(\frac{J_*}{J_{\rm s}} - 1\right). \tag{43}$$

Both frequencies are independent of $J_{\rm f}$ in the epicyclic limit. $\Omega_{\rm s}(J_{\rm s})$ has a resonance-independent form when expressed in terms of $(J_{\rm s}/J_*)$ and goes through zero at resonance, $J_{\rm s} = J_*$.

4.2.2. Posttransient Scar Widths

The resonant dynamics during the passage of the transient is described by the pendulum Hamiltonian of Equation (22), which is reproduced below:

$$H = \frac{1}{2}B_*(J_{\rm s} - J_*)^2 - \varepsilon_p A(\varepsilon t)\Phi_*\cos(\theta_{\rm s} - \xi_*).$$

Differentiating Equation (43), we find that

$$B_* = \frac{\partial\Omega_{\rm s}}{\partial J_{\rm s}}\bigg|_{J_{\rm s}=J_*} = -\frac{m\Omega_p}{J_*} < 0 \tag{44}$$

---

[8] For an $m = 1$ mode, this means that $\ell > -1/\sqrt{2}$, so there are no inner (i.e., $\ell = -1, -2, \ldots$) Lindblad resonances; for an $m = 2$ mode, $\ell > -\sqrt{2}$, so the inner (i.e., $\ell = -1$) Lindblad resonance exists but not the higher-order inner (i.e., $\ell = -2, -3, \ldots$) Lindblad resonances; and so on for higher m modes.

is independent of J_f in the epicyclic limit. When the potential perturbation arises mainly from the self-gravity of the perturbation to the disk surface density, then $\varepsilon_p = \eta\varepsilon_d$, where ε_d is the fractional surface density perturbation (which is more convenient to specify). $\Phi_* \sim -V_0^2$ is the (ℓ, m) Fourier coefficient of the normalized potential perturbation. We write it as $\Phi_*(J_f) = -(\pi V_0/4)^2 D_{\ell m}(J_f)$, where $D_{\ell m}(J_f)$ is a dimensionless, positive function.

As discussed in the previous section, the posttransient disk is also axisymmetric. The final DF is equal to the initial DF everywhere in phase space, except in narrow regions straddling different (ℓ, m) resonant lines. The half-widths of the scarred regions, given in Equation (26), are

$$\Delta J(J_f) = \frac{4}{\pi}\sqrt{\frac{\varepsilon_p \Phi_*(J_f)}{B_*}}$$
$$= \frac{V_0^2}{m\Omega_p}\sqrt{\left[1 + \sqrt{2}\,\frac{\ell}{m}\right]\eta\varepsilon_d\, D_{\ell m}(J_f)}. \quad (45)$$

At a given value of J_f in the (J_f, J_s) plane, the scar extends over a narrow strip, $|J_s - J_*| < \Delta J(J_f)$. The allowed values of J_f can be determined as follows. The minimum value of the fast action, j_0, satisfies Equation (33). Because the J_* of Equation (42) is independent of J_f, the solution to Equation (33) is just $j_0 = -\ell J_*$. Hence, $-\ell J_* \leqslant J_f$.

From Equation (32), the nonlinearity of the scar at the (ℓ, m) resonance is

$$\frac{\Delta J}{J_*} = \sqrt{\frac{\eta\varepsilon_d\, D_{\ell m}(J_f)}{[1 + \sqrt{2}\,(\ell/m)]}} \ll 1. \quad (46)$$

The $D_{\ell m}(J_f)$ diminish rapidly as $|\ell|$ increases, so the important resonances have small $|\ell|$. Our normalization is such that $D_{0m}(J_f)$ is an $O(1)$ function. But $D_{-1m}(J_f)$ and $D_{1m}(J_f)$ can be expected to be smaller because spiral density waves have the largest amplitudes near the CR and only extend about as far as the ILR or OLR; see, e.g., Figures 5 and 6 of SC14. We make an estimate of the scar widths at the principal resonances by setting $D_{0m} \sim 1$, $D_{-1m} \sim D_{1m} \sim 10^{-1}$. For a Mestel disk with $\{\beta = 35, Q = 1.5\}$ and an $m = 2$ transient with $\varepsilon_d = 10^{-2}$, we have

$$(\Delta J/J_*) \sim \{3.5 \times 10^{-2},\, 6 \times 10^{-2},\, 1.4 \times 10^{-2}\} \quad (47)$$

at the ILR, CR, and OLR, respectively.

4.3. Angular Momentum Transfer

We use Equation (35) to estimate the angular momentum absorbed by resonant stars from the transient. The initial DF near the (ℓ, m) resonance is $F_{in}(J_f, J_s) = F_0(J_f + \ell J_s, mJ_s)$, where $F_0(J_R, L_z)$ is the Mestel DF of Equation (38). This gives

$$F_{in}(J_f, J_s) = \frac{C}{mJ_s}\exp\left\{-\frac{\beta}{m}\left(\frac{J_f}{J_s} + \ell\right)\right\}. \quad (48)$$

Differentiating F_{in} with respect to J_s and setting $J_s = J_*$, we have

$$F_{in}^{(1)}(J_f) = \frac{C}{mJ_*^2}\left[\frac{\beta J_f}{mJ_*} - 1\right]\exp\left\{-\frac{\beta}{m}\left(\frac{J_f}{J_*} + \ell\right)\right\}. \quad (49)$$

Substituting Equations (49) and (45) into Equation (35),

$$\mathcal{L}_{abs} \simeq -\frac{8\pi^2}{3}mCJ_*\left\{\frac{\eta\varepsilon_d}{[1 + \sqrt{2}\,(\ell/m)]}\right\}^{3/2}$$
$$\times \int_{-\ell J_*}^{\infty} dJ_f\left[\frac{\beta J_f}{mJ_*} - 1\right]\exp\left\{-\frac{\beta}{m}\left(\frac{J_f}{J_*} + \ell\right)\right\}D_{\ell m}^{3/2}(J_f). \quad (50)$$

The functions $D_{\ell m}(J_f)$ determine the precise shapes of the scar boundaries in phase space. As discussed in item (c) following Equation (30), they are completely determined by the radial profile of the transient mode. $D_{\ell m}(J_f)$ can assume varied functional forms, depending on whether the transient is of spiral form or bar like. The functional forms must be either calculated in a model of observational data or taken from simulations. This is beyond the scope of this paper; we move forward by replacing $D_{\ell m}(J_f)$ by an effective resonance-dependent constant, $\bar{D}_{\ell m}$. Then, the J_f integral can be evaluated, and we obtain

$$\mathcal{L}_{abs} \sim \alpha_{\ell m}\mathcal{L}_{CR}, \quad (51)$$

where $L_{CR} = \eta V_0^5/2G\Omega_p^2$ is the total orbital angular momentum in stars of the unperturbed disk with $L_z \leqslant L_{CR} = V_0^2/\Omega_p$, and

$$\alpha_{\ell m} = \frac{4\beta}{3}\frac{\ell}{m}\left[1 + \sqrt{2}\,\frac{\ell}{m}\right]^{1/2}\{\eta\varepsilon_d\, \bar{D}_{\ell m}\}^{3/2} \quad (52)$$

is a resonance-dependent angular momentum absorption coefficient.

Because $\alpha_{\ell m}$ has the same sign as ℓ, we have $\mathcal{L}_{abs} < 0$ at all the inner Lindblad resonances, $\mathcal{L}_{abs} = 0$ at the CR, and $\mathcal{L}_{abs} > 0$ at all the outer Lindblad resonances. From footnote 2, the change in the epicyclic energies (per unit mass) of resonant stars ("heating") is $\Delta\mathcal{E}_{epi} \simeq (\ell/m)\kappa_*\mathcal{L}_{abs}$. There is no heating at the CR, whereas $\Delta\mathcal{E}_{epi} > 0$ at all Lindblad resonances. Over its passage, the transient nonaxisymmetric mode has transferred angular momentum from the inner to the outer Lindblad resonances while heating up stars, which is in the same sense as the linear theory of Lynden-Bell & Kalnajs (1972) discussed in Section 2.3. But $\mathcal{L}_{abs} \sim O(\varepsilon_d^{3/2})$, which is larger than the $O(\varepsilon_d^2)$ change expected from the linear theory.

4.4. Scars in Phase Space and Real Space

The angular momentum exchanges described above are a result of mass transfer across resonant surfaces. As discussed in Section 3.3, the basic quantity describing these changes in phase space is the DF of a scar, $\Delta F(J_f, J_s)$, given by Equation (30) or (31). In Section 4.4.1, we derive an explicit expression for ΔF at any (ℓ, m) resonance in a cool Mestel disk. The global rearrangement of mass in phase space is best appreciated when ΔF is plotted as a function of the global coordinates (J_R, L_z). This is done in Figure 4 by assuming that the scar width is a constant, as was used to derive Equation (51) for $\mathcal{L}_{abs}$. In Section 4.4.2, we integrate ΔF to obtain $\Delta\Sigma(R)$, the axisymmetric perturbation to the disk surface density.

4.4.1. Global Changes in the DF

The DF of the scar, $\Delta F(J_f, J_s)$, at the (ℓ, m) resonance of a cool Mestel disk can be obtained by using Equation (49) in Equation (31). ΔF is zero for $|J_s - J_*| \geqslant \Delta J(J_f)$, where J_* and
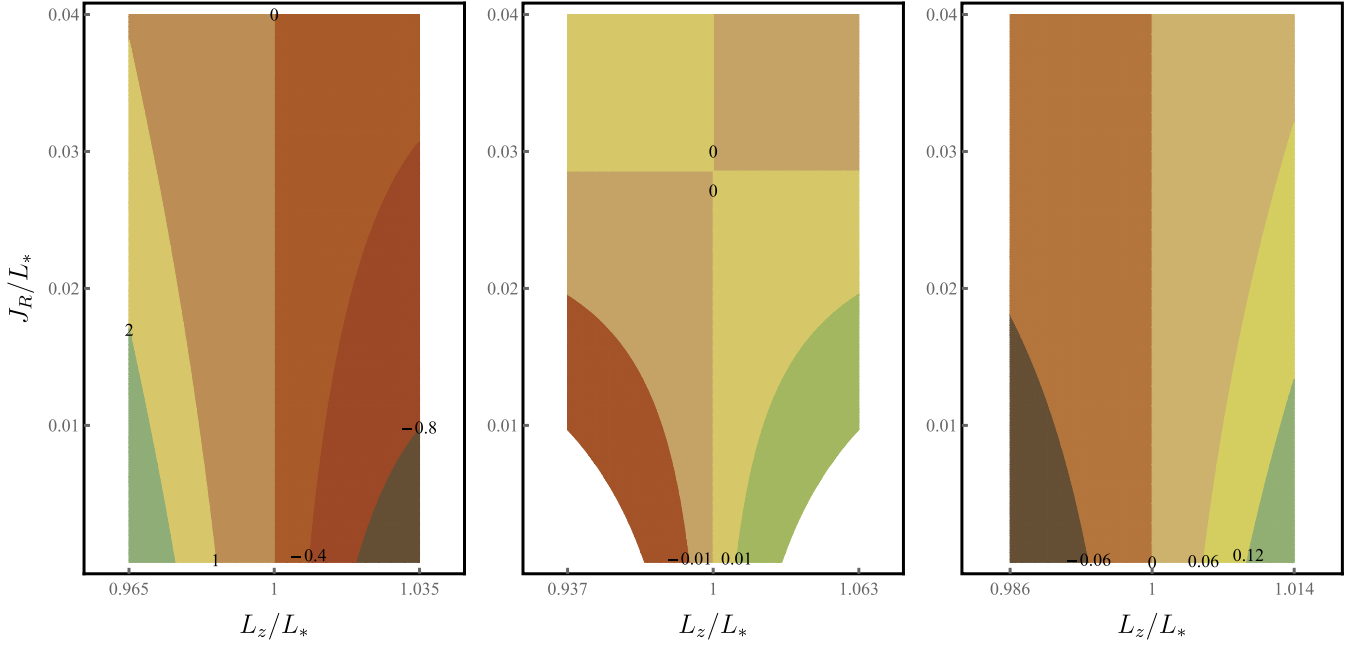
Figure 4. DFs of scars at the principal resonances in the (J_R, L_z) plane, after the passage of an $m = 2$ adiabatic transient mode. The left panel is for ILR near $L_{ILR} = 0.29(V_0^2/\Omega_p)$, the central panel is for CR near $L_{CR} = V_0^2/\Omega_p$, and the right panel is for OLR near $L_{OLR} = 1.7(V_0^2/\Omega_p)$. Isocontours of $\Delta F_{\ell m}(J_R, L_z)$ of Equation (56) are drawn in units of $C\Omega_p/V_0^2$, for $\beta = 35$ and $\Delta L/L_* = \{0.035, 0.063, 0.014\}$ as in Equation (47). $\Delta F_{\ell m} = 0$ in the white regions outside the scar. J_R and L_z are naturally measured in units of L_*, which is equal to $\{L_{ILR}, L_{CR}, L_{OLR}\}$ in the three panels.

$\Delta J(J_f)$ are given in Equations (42) and (45). For $|J_s - J_*| < \Delta J(J_f)$, the DF of the scar is

$$\Delta F \simeq \frac{C}{mJ_*^2}\left[1 - \frac{\beta J_f}{mJ_*}\right]\exp\left\{-\frac{\beta}{m}\left(\frac{J_f}{J_*} + \ell\right)\right\}(J_s - J_*). \quad (53)$$

Within the scarred region, ΔF is an odd function of $(J_s - J_*)$, so the mass in every (ℓ, m) scar is zero. The equation of the resonant line in the (J_R, L_z) plane is $L_z = L_*$, where

$$L_* = mJ_* = \frac{V_0^2}{\Omega_p}\left[1 + \sqrt{2}\frac{\ell}{m}\right]. \quad (54)$$

The half-width of the scar, $\Delta L = m\Delta J(J_f)$, depends on (J_R, L_z) because $J_f = J_R - (\ell/m)L_z$:

$$\Delta L(J_R, L_z) = m\Delta J\left(J_R - \frac{\ell}{m}L_z\right)$$
$$= \frac{V_0^2}{\Omega_p}\sqrt{\left[1 + \sqrt{2}\frac{\ell}{m}\right]\eta\varepsilon_d \, D_{\ell m}\left(J_R - \frac{\ell}{m}L_z\right)}. \quad (55)$$

We write the DF of the scar, $\Delta F(J_f, J_s) = \Delta F_{\ell m}(J_R, L_z)$, to emphasize its dependence on (ℓ, m). $\Delta F_{\ell m}$ vanishes for $|L_z - L_*| \geqslant \Delta L$. For $|L_z - L_*| < \Delta L$, it can be written as a function of (J_R, L_z) by substituting $J_f = J_R - (\ell/m)L_z$ and $J_s = L_z/m$ in Equation (53):

$$\Delta F_{\ell m}(J_R, L_z) \simeq \frac{C}{L_*^2}\left[1 - \beta\left(\frac{J_R}{L_*} - \frac{\ell}{m}\frac{L_z}{L_*}\right)\right]$$
$$\times \exp\left\{-\beta\left[\frac{J_R}{L_*} - \frac{\ell}{m}\left(\frac{L_z}{L_*} - 1\right)\right]\right\} \times \left(\frac{L_z}{L_*} - 1\right). \quad (56)$$

We still need to specify a functional form for $D_{\ell m}(J_f)$. As discussed in Section 4.3, this requires information on the radial profile of the transient mode. We made the simplifying assumption $D_{\ell m}(J_f) \rightarrow \bar{D}_{\ell m}$ and derived Equation (51) for $\mathcal{L}_{abs}$. The discussion following this equation provides some assurance that the resulting properties of $\mathcal{L}_{abs}$ are consistent with what may be expected of angular momentum exchanges between a nonaxisymmetric mode and resonant stars. But it is a poor representation of the shape of a scar. Henceforth, we use

$$\Delta L = \frac{V_0^2}{\Omega_p}\sqrt{\left[1 + \sqrt{2}\frac{\ell}{m}\right]\eta\varepsilon_d \, \bar{D}_{\ell m}}, \quad (57)$$

which is useful in providing a global picture of resonant mass shifts and in calculating the perturbation to the surface density. In Figure 4, we plot $\Delta F_{\ell m}(J_R, L_z)$ near the principal resonances of an $m = 2$ transient. The specific functional forms will be used in the rest of this paper; for the present, we note some overall qualitative features:

1. Mass has shifted to lower L_z at the ILR (left panel) and to higher L_z at the OLR (right panel), corresponding to $\mathcal{L}_{abs} < 0$ at the ILR and $\mathcal{L}_{abs} > 0$ at the OLR from Equation (51). Because the J_f of every star is constant, the mass shift is due to the changes in the actions of the resonant stars, with $\delta J_R = -\delta L_z/2$ at the ILR and $\delta J_R = \delta L_z/2$ at the OLR; see footnote 2.

2. $\Delta F_{-1,2}$ is larger than $\Delta F_{1,2}$, because the Mestel DF is larger at the ILR than the OLR; see Figure 3. If this overall difference in magnitudes is factored out, we see that the isocontours of ΔF_{-1m} and $\Delta F_{1,m}$ are, very roughly, mirror images of each other, when (J_R, L_z) are expressed in units of the corresponding L_* (i.e., L_{ILR} and L_{OLR}, respectively).

3. The scar at the CR (central panel) is very different. ΔF_{0m} is an odd function of $(L_z - L_{CR})$ and has a smaller magnitude.

11

J_R is conserved during the mass shifts, because it is equal to the fast action at the CR. Moreover, $\delta L_z > 0$ for $J_R < L_*/\beta \simeq 0.03 L_*$, and $\delta L_z < 0$ for $J_R > L_*/\beta \simeq 0.03 L_*$, with $\mathcal{L}_{abs} = 0$ from Equation (51). The changes in L_z lead to the radial mixing of stars (Sellwood & Binney 2002); ΔF_{0m} gives a phase-space picture of this process for a transient mode.

4.4.2. Surface Densities of Scars

The DF of each scar, $\Delta F_{\ell m}(J_R, L_z)$, gives rise to an axisymmetric perturbation in the disk surface density, $\Delta \Sigma_{\ell m}(R)$. This is obtained by integrating $\Delta F_{\ell m}$ over velocity space:

$$\Delta \Sigma_{\ell m}(R) = \frac{1}{R} \int dL_z \, dp_R \, \Delta F_{\ell m}(J_R, L_z), \qquad (58)$$

where Equation (37) may be used express J_R as a function of (R, p_R, L_z).

Because the DF of the scar is localized around $L_z \simeq L_*$, we expect the surface density of the scar, $\Delta \Sigma_{\ell m}(R)$, to be localized around the resonant radius,

$$R_* = \frac{L_*}{V_0} = \frac{V_0}{\Omega_p} \left[1 + \sqrt{2} \frac{\ell}{m} \right]. \qquad (59)$$

The standard epicyclic approximation ($R_{epi} \ll R_*$), which was sufficient to calculate $\Sigma_0(R)$ from $F_0(J_R, L_z)$ for the unperturbed disk, cannot be applied directly to evaluate the integral in Equation (58). This is because ΔL, the half-width of the scar in phase space, introduces a new small radial scale in the problem:

$$\Delta R = \frac{\Delta L}{V_0} = \frac{V_0}{\Omega_p} \sqrt{\left[1 + \sqrt{2} \frac{\ell}{m} \right] \eta \varepsilon_d \, \bar{D}_{\ell m}}. \qquad (60)$$

Comparing ΔR with the typical epicyclic radius of orbits in the scar,

$$\frac{\Delta R}{R_{epi}} = 2^{1/4} \sqrt{\beta} \frac{\Delta R}{R_*} = 2^{1/4} \sqrt{\beta} \frac{\Delta J}{J_*}, \qquad (61)$$

where $(\Delta J/J_*)$ is the nonlinearity of the scar given in Equation (46). For a Mestel disk with $\{\beta = 35, Q = 1.5\}$ and an $m = 2$ transient with $\varepsilon_d = 10^{-2}$, used in the estimates of $(\Delta J/J_*)$ in Equation (47), we have

$$\Delta R / R_{epi} \sim \{0.25, 0.42, 0.1\} \qquad (62)$$

at the ILR, CR, and OLR, respectively.

With this estimate in hand, we see that the appropriate generalization of the epicyclic approximation is the ordering $\Delta R \ll R_{epi} \ll R_*$, even though it is not so good at the ILR and CR. This is applied to the integral of Equation (58) in Appendix B.1 to obtain

$$\Delta \Sigma_{\ell m}(R) = \mu_{\ell m} \Sigma_0(R_*) S(R), \qquad (63)$$

where $\mu_{\ell m}$ is a resonance-dependent dimensionless number, $\Sigma_0(R_*) = \eta V_0^2 / 2\pi G \, R_*$ is the surface density of the unperturbed Mestel disk at R_*, $S(R)$ is an $O(1)$ dimensionless function that contains all the R-dependence, and

$$\mu_{\ell m} = \frac{2\pi \beta^{1/4}}{3Q^{3/2}} \left(\frac{3}{2} + \beta \frac{\ell}{m} \right) \left[\frac{\varepsilon_d \, \bar{D}_{\ell m}}{1 + \sqrt{2} \, (\ell/m)} \right]^{3/2} \qquad (64)$$

determines the magnitude and sense of mass shifts due to the surface density perturbation. For the same parameter values

used for the estimates in Equation (61),

$$\mu_{\ell m} \sim \{-9 \times 10^{-3}, 4 \times 10^{-3}, 7 \times 10^{-4}\}, \qquad (65)$$

at the ILR, CR, and OLR, respectively; it is negative at the ILR and positive at the CR and OLR. The shape function

$$S(R) \sim \frac{R_*}{R} \left(\frac{R - R_*}{R_{epi}} \right) \exp \left\{ -\frac{1}{2} \left(\frac{R - R_*}{R_{epi}} \right)^2 \right\}$$

$$\times \left[1 - \frac{1}{3 + 2\beta(\ell/m)} \left(\frac{R - R_*}{R_{epi}} \right)^2 \right] \qquad (66)$$

is a function of (R/R_*) because $R_{epi} \propto R_*$. The Gaussian factor implies that the radial scale of the scar is the local epicyclic radius.

The fractional surface density, $\Delta \Sigma_{\ell m}(R)/\Sigma_0(R_*) = \mu_{\ell m} S(R)$, is plotted at the principal resonances in Figure 5. This illustrates the following general properties of the surface densities of scars.

1. $\Delta \Sigma_{\ell m}(R)$ vanishes at R_* and shows opposite behavior inside/outside R_*; more precisely, $R \, \Delta \Sigma_{\ell m}(R)$ is an odd function of $(R - R_*)$. The total mass in the scar, $2\pi \int_0^\infty dR \, R \, \Delta \Sigma_{\ell m}(R)$, is given by the sum of two terms; one of them is $\propto \int_{(-R_*/R_{epi})}^\infty dx \, x \exp(-x^2/2)$ and the other is $\propto \int_{(-R_*/R_{epi})}^\infty dx \, x^3 \exp(-x^2/2)$. Because the integrands are odd functions of x, both the integrals are vanishingly small in the epicyclic limit, $R_* \gg R_{epi}$. So the total mass in every scar is zero, as expected.

2. Because $\Delta R \ll R_{epi}$, the width of the scar in real space is due to epicyclic broadening, with the information about the "intrinsic" width, ΔR, now contained in the constant $\mu_{\ell m}$.

3. The sign of $\mu_{\ell m}$ determines the sense of mass shifts across R_*. It is radially inward when $(3/2 + \beta \ell/m) < 0$ and radially outward when $(3/2 + \beta \ell/m) > 0$. Hence, mass shifts outward at the CR and, for $\beta/m > 3/2$ for m not too large, inward/outward at the ILR/OLR. The mass shifts are largest at corotation and cause radial mixing of stars (Sellwood & Binney 2002), even though the angular momentum absorbed at the CR is, to leading order, zero from Equation (51).

5. Suppressed Torques in the Final Disk

In Section 3, we considered the nonlinear transformation of a smooth initial axisymmetric DF to a scarred final axisymmetric DF, due to the passage of an adiabatic, nonaxisymmetric transient mode with angular wavenumber $m > 0$ and pattern speed Ω_p. The final DF is equal to the initial DF everywhere in phase space, except in the vicinity of resonances, as given in Equation (27). Both are axisymmetric DFs, but the initial DF is smooth, whereas the final DF is flattened near resonances; see Figure 2. In this section, we demonstrate that this is responsible for the very different responses of the two DFs to any new linear perturbation with the same angular wavenumber $m > 0$ and pattern speed Ω_p as the original transient mode.

In Section 5.1, we formulate the problem of comparing the LBK torques, in the initial and final DFs, by casting the formulae of Section 2.3 in terms of slow and fast action-angle variables. This reveals a very interesting property that is entirely a result of the phase-space structure of the final DF: when the self-gravity due to the scars is ignored in the final
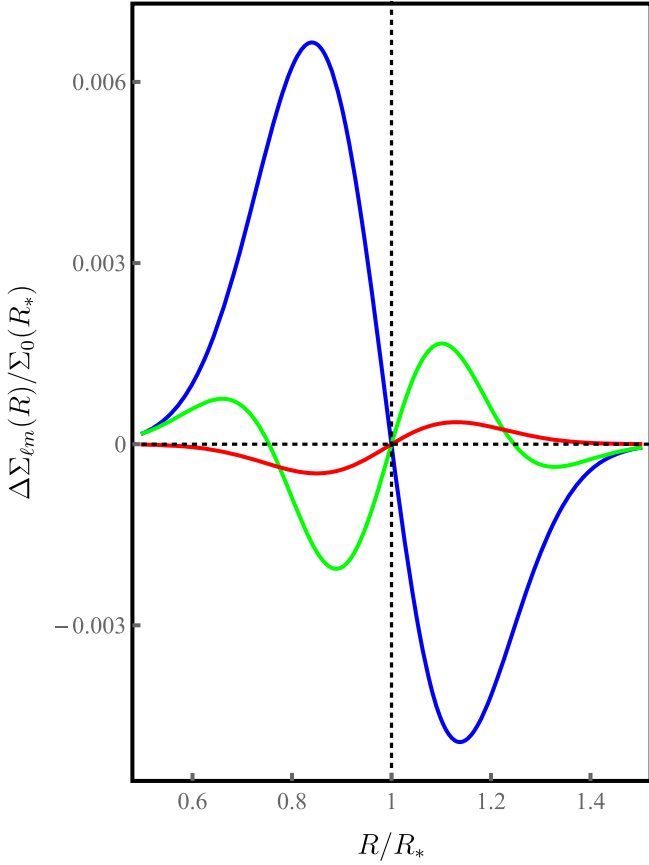
Figure 5. Radial profiles of the fractional surface densities of scars at the principal resonances. Blue/green/red curves correspond to ILR/CR/OLR, respectively. Parameter values used are the same as in Figure 4, with $\mu_{\ell m}$ taken from Equation (65). Abscissa is R/R_*, where R_* is equal to $R_{\rm ILR} = 0.29(V_0/\Omega_{\rm p})$, $R_{\rm CR} = V_0/\Omega_{\rm p}$, and $R_{\rm OLR} = 1.7(V_0/\Omega_{\rm p})$ for the three curves.

axisymmetric disk, all of the LBK torques, $\mathcal{T}'_{\ell m}$, vanish. Hence, the extra radial acceleration due to the gravity of the scars must be considered. This causes small changes in the radial and angular frequencies and lead to slight shifts of resonances, which are calculated in Section 5.2 for the scarred Mestel disk of Section 4. In Section 5.3, we derive a formula $\mathcal{T}'_{\ell m}$, which is nonzero but still much smaller than $\mathcal{T}_{\ell m}$, the torque in the initial disk. The consequences of suppressed resonant torques for mode renewal are then addressed.

5.1. LBK Torques in the Initial and Final DFs—I

Here we discuss the LBK torques acting on the initial and final DFs, due to a linear mode with potential perturbation

$$\Psi_1 = \varepsilon_{\rm s} \exp(\gamma t)\Psi_a(R)\cos\{m(\phi - \Omega_{\rm p}t) + \zeta_a(R)\}. \quad (67)$$

Because the mode is linear, $\varepsilon_{\rm s} \ll 1$ is infinitesimal, and $\gamma > 0$ for a perturbation that is applied gradually in time. $\Psi_a(R)$ and $\zeta_a(R)$ give the radial profile of the mode amplitude and phase and can be of general form.

We consider first the initial disk with DF, $F_0(J_R, L_z)$, and surface density profile $\Sigma_0(R)$. The gravity of $\Sigma_0(R)$ (and any external source such as a dark halo) gives rise to a radial acceleration profile, $a_0(R)$, which determines the radial and angular frequencies, $\Omega_R(J_R, L_z)$ and $\Omega_\phi(J_R, L_z)$, given in Equation (7). The torque due to a marginally growing, i.e.,

$\gamma \to 0_+$, Ψ_1 at the (ℓ, m) resonance is given by Equation 13(b):

$$\mathcal{T}_{\ell m} = -8\pi^3\varepsilon_{\rm s}^2 m \int dJ_R dL_z \left(\ell\frac{\partial F_0}{\partial J_R} + m\frac{\partial F_0}{\partial L_z}\right)$$
$$\times \delta(\ell\Omega_R + m\{\Omega_\phi - \Omega_{\rm p}\})|\widetilde{\Psi}_{\ell m}(J_R, L_z)|^2, \quad (68)$$

where $\widetilde{\Psi}_{\ell m}(J_R, L_z)$ are Fourier coefficients corresponding to Ψ_1. Because the contribution to the integral is only from the resonant curve in the (J_R, L_z) plane, we can rewrite the integral in terms of the fast and slow action-angle variables, which are useful coordinates in the vicinity of the resonant line. From Equation (24), the initial DF is $F_{\rm in}(J_{\rm f}, J_{\rm s}) = F_0(J_{\rm f} + \ell J_{\rm s}, m J_{\rm s})$. Defining $\widehat{\Psi}_{\ell m}(J_{\rm f}, J_{\rm s}) = \widetilde{\Psi}_{\ell m}(J_{\rm f} + \ell J_{\rm s}, mJ_{\rm s})$, we have

$$\mathcal{T}_{\ell m} = -8\pi^3\varepsilon_{\rm s}^2 m^2 \int dJ_{\rm f} \; dJ_{\rm s}\frac{\partial F_{\rm in}}{\partial J_{\rm s}}\delta(\Omega_{\rm s})|\widehat{\Psi}_{\ell m}(J_{\rm f}, J_{\rm s})|^2. \quad (69)$$

We write $\delta(\Omega_{\rm s}) = \delta(J_{\rm s} - J_*)/|B_*(J_{\rm f})|$, where $J_{\rm s} = J_*(J_{\rm f})$ is the equation of the resonant curve of Equation (20), and $B_*(J_{\rm f}) = (\partial\Omega_{\rm s}/\partial J_{\rm s})_{J_{\rm s}=J_*}$ as given for the pendulum Hamiltonian of Equation (22). Integrating over $J_{\rm s}$, we obtain a compact expression for the resonant torque:

$$\mathcal{T}_{\ell m} = -8\pi^3\varepsilon_{\rm s}^2 m^2 \int_{j_0}^\infty dJ_{\rm f}\frac{F_{\rm in}^{(1)}(J_{\rm f})}{|B_*(J_{\rm f})|}|\widehat{\Psi}_{\ell m}(J_{\rm f}, J_*(J_{\rm f}))|^2, \quad (70)$$

where $F_{\rm in}^{(n)}(J_{\rm f}) = (\partial^n F_{\rm in}/\partial J_{\rm s}^n)_{J_{\rm s}=J_*}$. The evaluation of $\mathcal{T}_{\ell m}$ has been reduced to a one-dimensional integral over $J_{\rm f}$, from its minimum value of j_0 in Equation (33) to ∞. This formula is valid for a smooth initial DF of general form and not restricted to the cool Mestel disk.

We want to derive a similar expression for the torque exerted by $\Psi_1(R, \phi, t)$ on the scarred disk, described by the final (posttransient) DF. The final DF is equal to the sum of the initial DF and the DFs of scars at all the (ℓ, m) resonances. So, the surface density profile of the final disk is

$$\Sigma(R) = \Sigma_0(R) + \sum_\ell \Delta\Sigma_{\ell m}(R), \quad (71)$$

where $\Delta\Sigma_{\ell m}(R)$ is the surface density due to the scar at the (ℓ, m) resonance. The radial acceleration profile in the final disk is

$$a(R) = a_0(R) + \sum_\ell \Delta a_{\ell m}(R), \quad (72)$$

where $\Delta a_{\ell m}(R)$ is the radial acceleration due to the gravity of $\Delta\Sigma_{\ell m}(R)$. The magnitude of these changes is of order the fractional perturbation, $\Delta a_{\ell m}/a_0 \sim \eta\,\Delta\Sigma_{\ell m}/\Sigma_0$.

For the cool Mestel disk, $\Delta a_{\ell m}/a_0 \sim \eta\,\mu_{\ell m}$ is very small; see Equation (78). So, it is reasonable to begin with the lowest-order estimate of resonant torques in the final disk, by setting $\mu_{\ell m} \to 0$. This is equivalent to ignoring $\Delta a_{\ell m}(R)$, so $a(R) \to a_0(R)$. Then, the action-angle variables for the final disk, (J_R, L_z), as well as $\Omega_R(J_R, L_z)$ and $\Omega_\phi(J_R, L_z)$, are the same as for the initial disk. Hence, the resonant curves, determined by $\ell\Omega_R + m\{\Omega_\phi - \Omega_{\rm p}\} = 0$, are also the same for the two disks.

As earlier, we can introduce $(J_{\rm f}, J_{\rm s})$ variables near the (ℓ, m) resonance. Then, the resonant torque due to Ψ_1 in the final disk

is

$$\mathcal{T}'_{\ell m} = -8\pi^3 \varepsilon_s^2 m^2 \int dJ_f \ dJ_s \frac{\partial F_{fin}}{\partial J_s} \delta(\Omega_s) |\widehat{\Psi}_{\ell m}(J_f, J_s)|^2$$

$$= -8\pi^3 \varepsilon_s^2 m^2 \int_{j_0}^{\infty} dJ_f \frac{F_{fin}^{(1)}(J_f)}{|B_*(J_f)|} |\widehat{\Psi}_{\ell m}(J_f, J_*(J_f))|^2, \quad (73)$$

where $F_{fin}^{(1)}(J_f) = (\partial F_{fin}/\partial J_s)_{J_s = J_*}$. We can use Equation (29) to express $F_{fin}(J_f, J_s)$ in terms of $F_{in}(J_f, J_s)$. Then, $F_{fin}^{(1)}(J_f) = F_{in}^{(2)}(J_f)(J_s - J_*)|_{J_s = J_*} = 0$, which can also be seen from Figure 2, where the final, flattened DF has zero slope at resonance. Then, $\mathcal{T}'_{\ell m} = 0$, so the linear mode exerts no torque on disk stars. This conclusion holds for a scarred, final DF of general form and not restricted to the scarred Mestel disk.

The vanishing of all resonant torques is due to a conjunction of two ingredients: (i) the limit $\mu_{\ell m} \rightarrow 0$, which ensured that the resonant lines in the final disk coincide exactly with those in the initial disk, and (ii) that the final DF has exactly zero slope at the scar center. When $\mu_{\ell m} \neq 0$, the resonant lines in the final disk will be slightly shifted from those in the initial disk, where the slope of the final DF would be nonzero, resulting in nonzero $\mathcal{T}'_{\ell m}$.

5.2. Resonance Shifts in the Scarred Mestel Disk

Because the $\mu_{\ell m} \rightarrow 0$ theory gives a vanishing result for $\mathcal{T}'_{\ell m}$, we are obliged to calculate to the next order and consider a small but nonzero $\mu_{\ell m}$, such as those given in Equation (65). We want to calculate the orbital and epicyclic frequencies, $\Omega(L_z)$ and $\kappa(L_z)$, inside the scars of the final disk, which are defined in terms of $a(R)$, the radial acceleration profile in the scarred disk. We must first determine the new guiding-center radius, $R'_g(L_z)$, by solving $L_z^2 = -R^3 a(R)$. Then,

$$\Omega^2(L_z) = -\frac{a(R)}{R} \bigg|_{R=R'_g}, \quad (74a)$$

$$\kappa^2(L_z) = -\frac{1}{R^3} \frac{d}{dR}[R^3 a(R)] \bigg|_{R=R'_g}, \quad (74b)$$

gives the frequencies in the scarred Mestel disk. From Equation (72), $a(R)$ is the sum of the known function $a_0(R) = -V_0^2/R$ and $\Delta a_{\ell m}(R)$ at all resonances, which we now calculate.

5.2.1. $\Delta a_{\ell m}(R)$ within a Scar

From Figure 5, we see that $\Delta \Sigma_{\ell m}(R)$ is concentrated within an annulus of half-width R_{epi} about the resonant radius, outside which its amplitude falls rapidly. So, at distances much larger than its width, $|R - R_*| \gg R_{epi}$, the scar appears as two concentric circular wires near R_* with equal and opposite masses. $\Delta a_{\ell m}(R)$ is due mainly to the (dipolar) far field and is small because of close cancellations between the attraction and repulsion of the two wires. Because the resonant radii R_* are well separated for different ℓ, the field of one scar on another can be ignored in a first approximation. Hence, the dominant contribution to $\Delta a_{\ell m}(R)$ near a scar is due to its self-gravity.[9]

---

[9] A scar can be thought of as a ring-like "gravitational capacitor" in real space, with its external field smaller than its internal field. Equation (75) relates the internal field to the surface density profile of the scar.

We have

$$\Delta a_{\ell m}(R) \simeq 2G \int_0^{\infty} dR' \frac{\Delta \Sigma_{\ell m}(R')}{R' - R}, \quad (75)$$

where $\Delta \Sigma_{\ell m}(R)$ is given in Equation (63). This formula is exactly equivalent to the familiar relationship between the potential and surface density of tightly wound spiral patterns—see Equations (6.29) and (6.30) of Binney & Tremaine (2008).

This integral can be expressed in terms of special functions, but we do not need these for the purposes of calculating frequency shifts close to resonance. From Equation (74), we see that $\Omega(L_z)$ depends on $\Delta a_{\ell m}$, whereas $\kappa(L_z)$ depends on both $\Delta a_{\ell m}$ and $d(\Delta a_{\ell m})/dR$. Hence, we require $\Delta a_{\ell m}(R)$ only to first order in $(R - R_*)/R_*$. We calculate this in Appendix B.2 to obtain

$$\Delta a_{\ell m}(R) \simeq \delta_{\ell m} \frac{V_0^2}{R_*} \left[1 - \left(\frac{R - R_*}{R_*}\right)\right], \quad (76)$$

where

$$\delta_{\ell m} = \frac{1}{Q}\sqrt{\frac{2\pi}{\beta}}\left[1 - \frac{1}{3 + 2\beta(\ell/m)}\right]\mu_{\ell m} \quad (77)$$

is a dimensionless resonance-dependent number that is a measure of the fractional difference in the radial acceleration near R_*, between the final and initial Mestel disks. For the same parameter values used for the estimates of $\mu_{\ell m}$ in Equation (65), we have

$$\delta_{\ell m} \sim \{-2.6 \times 10^{-3}, 7 \times 10^{-4}, 2 \times 10^{-4}\} \quad (78)$$

at the ILR, CR, and OLR, respectively.

5.2.2. Frequency Profiles within a Scar

Having determined $\Delta a_{\ell m}(R)$, we can calculate the guiding-center radius, $R'_g(L_z)$, by solving $L_z^2 = (V_0 R)^2 - R^3 \Delta a_{\ell m}(R)$. We require this only within the scar in phase space, i.e., for $|L_z - L_*| < \Delta L$. Solving to first order in $\delta_{\ell m}$, we get $R'_g(L_z) \simeq [1 + (\delta_{\ell m}/2)](L_z/V_0)$. The fractional shift in the guiding-center radius, $\delta_{\ell m}/2$, is negative at the ILR and positive at the CR and the OLR. The frequencies can now be calculated by using $a(R) = -(V_0^2/R) + \Delta a_{\ell m}(R)$ in Equation (74):

$$\Omega^2(L_z) = \Omega_0^2(L_z) - \frac{\Delta a_{\ell m}(R)}{R}\bigg|_{R=R'_g}, \quad (79a)$$

$$\kappa^2(L_z) = \kappa_0^2(L_z) - \frac{1}{R^3}\frac{d}{dR}[R^3 \Delta a_{\ell m}(R)]\bigg|_{R=R'_g}. \quad (79b)$$

We can get the frequencies to first order in $\delta_{\ell m}$ by setting $R = L_z/V_0$ in the second terms on the right side. Using Equation (76) for $\Delta a_{\ell m}(R)$, we obtain

$$\Omega(L_z) \simeq \frac{V_0^2}{L_z}\left[1 - \frac{1}{2}\delta_{\ell m}\right], \qquad \kappa(L_z) \simeq \sqrt{2}\,\Omega(L_z). \quad (80)$$

The slow frequency within the scar is

$$\Omega'_s(J_s) = \ell\kappa + m(\Omega - \Omega_p)$$

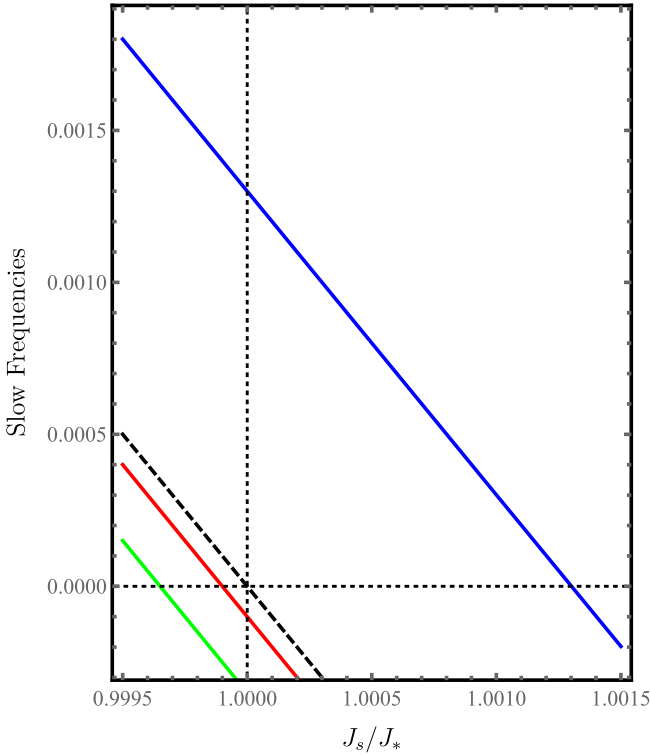$$\simeq m\Omega_p\left(\frac{J_*}{J_s} - 1 - \frac{1}{2}\delta_{\ell m}\right). \quad (81)$$

14

Figure 6. Slow frequencies near resonances in the initial and final Mestel disks, measured in units of $m\Omega_p$. The dashed black line is Ω_s of Equation (43). The solid blue/green/red curves are for Ω_s' of Equation (81), at the ILR/CR/OLR, respectively. Parameter values used are the same as in earlier figures, with $\delta_{\ell m}$ taken from Equation (78).

Similar to the slow frequency in the initial Mestel disk, $\Omega_s(J_s)$ of Equation (43), $\Omega_s'(J_s)$ is a function of (J_s/J_*). But its functional form is resonance dependent, as can be seen in Figure 6. Indeed, the difference between Ω_s' and Ω_s is equal to $-m\Omega_p\delta_{\ell m}/2$, which is positive at the ILR and negative at the CR and the OLR.

The equation of the (ℓ, m) resonant line in the final disk is given by $J_s = J_*'$, where $\Omega_s'(J_*') = 0$. Solving this to first order in $\delta_{\ell m}$, we obtain

$$J_*' \simeq [1 - (\delta_{\ell m}/2)]J_*, \qquad (82)$$

which shows that resonant lines undergo shifts $\delta J_* = -(\delta_{\ell m}/2)J_*$. At the shifted resonant location, the quantity

$$B_*' = \left.\frac{\partial \Omega_{ss}'}{\partial J_s}\right|_{J_s = J_*'} \simeq -\frac{m\Omega_p}{J_*}[1 + \delta_{\ell m}] = B_*[1 + \delta_{\ell m}]. \quad (83)$$

For the same values of parameters as earlier, the fractional shifts at the principal resonances are

$$(\delta J_*/J_*) \sim \{1.3 \times 10^{-3}, -3.5 \times 10^{-4}, -10^{-4}\}. \qquad (84)$$

This is positive at the ILR and negative at the CR and the OLR; see Figure 6. The scar half-widths, ΔJ of Equation (47), are two orders of magnitude larger than the shifts. Because $|\delta J_*| \ll \Delta J$, the shifted resonant lines lie well within the scars where the final DF is flattened. Below we show that the nonzero shifts of the ILR/CR/OLR give rise to nonzero resonant torques in the final disk; as the shifts are small, the torques are weaker than in the initial disk.

5.3. LBK Torques in the Initial and Final DFs—II

We are now in a position to compare resonant torques in the initial and final disks, due to the linear mode $\Psi_1(R, \phi, t)$ of Equation (67), taking into account the self-gravity of the scars. In order to make quantitative estimates, we use the smooth and scarred Mestel disks.

5.3.1. Torques in the Smooth Mestel Disk

From Equation (70), the resonant torque in the smooth Mestel disk is

$$\mathcal{T}_{\ell m} = -8\pi^3\varepsilon_s^2 m^2 \int_{-\ell J_*}^{\infty} dJ_f \frac{F_{in}^{(1)}(J_f)}{|B_*|} |\widehat{\Psi}_{\ell m}(J_f, J_*)|^2, \qquad (85)$$

where $|B_*| = m\Omega_p/J_*$ and $F_{in}^{(1)}(J_f)$ is given in Equation (49). It is convenient to use the integration variable $x = (\beta/m)(J_f/J_* + \ell)$ and the Fourier coefficient $\psi_{\ell m}(x, \beta) = \widehat{\Psi}_{\ell m}(J_*(mx/\beta - \ell), J_*)$. Then,

$$\mathcal{T}_{\ell m} = 8\pi^3\varepsilon_s^2 \frac{mC}{\beta\Omega_p} \int_0^{\infty} dx\, W_{\ell m}(x, \beta)|\psi_{\ell m}(x, \beta)|^2, \qquad (86)$$

where

$$W_{\ell m}(x, \beta) = \left\{1 + \frac{\beta\ell}{m} - x\right\} \exp(-x) \qquad (87)$$

is the torque weight function for the smooth Mestel disk, plotted in the left panel of Figure 7, at the principal resonances.

5.3.2. Torques in the Scarred Mestel Disk

We will derive an analogous equation for the resonant torques due to $\Psi_1(R, \phi, t)$ on the scarred Mestel disk, taking into account the shifts in frequencies and resonance locations due to the self-gravity of the scars, derived in Section 5.2. Let (J_R', L_z') be the action variables in the scarred disk. $L_z' = L_z$, but $J_R' \neq J_R$ of Equation (37) within the scar. Here, it is given by

$$J_R' \simeq \frac{p_R^2}{2\kappa(L_z)} + \frac{\kappa(L_z)}{2}[R - R_g'(L_z)]^2, \qquad (88)$$

where $\kappa(L_z)$ is given in Equation (80) and $R_g'(L_z) \simeq [1 + (\delta_{\ell m}/2)]R_g(L_z)$. The slow and fast actions near the (ℓ, m) resonance are $J_f' = J_R' - (\ell/m)L_z'$ and $J_s' = L_z'/m$. Because κ and R_g' differ from κ_0 and R_g by $O(\delta_{\ell m})$, Equation (88) gives $J_R' = J_R + O(\delta_{\ell m})$. Then, $J_f' = J_f + O(\delta_{\ell m})$, whereas $J_s' = J_s$ remains unchanged. The $O(\delta_{\ell m})$ shift in the fast action is unimportant, and we can set $(J_f', J_s') \rightarrow (J_f, J_s)$.

The resonant torque is

$$\mathcal{T}_{\ell m}' \simeq -8\pi^3\varepsilon_s^2 m^2 \int dJ_f\, dJ_s \frac{\partial F_{fin}}{\partial J_s} \delta(\Omega_s')|\widehat{\Psi}_{\ell m}(J_f, J_s)|^2, \quad (89)$$

where $\Omega_s'(J_s)$ is the slow frequency of Equation (81), and $F_{fin}(J_f, J_s)$ is given in terms of the initial DF by Equation (29). We want to calculate the integrand to leading order in $\delta_{\ell m}$:

$$\delta(\Omega_s') = \frac{\delta(J_s - J_*')}{|B_*'|} \simeq \frac{\delta(J_s - J_*')}{|B_*|}[1 - \delta_{\ell m}],$$

where we have used Equation (83) for B_*'. From Equations (47) and (84), we know that the shifted position of the resonance lies well inside the scar in phase space. Using this in Equation (29),
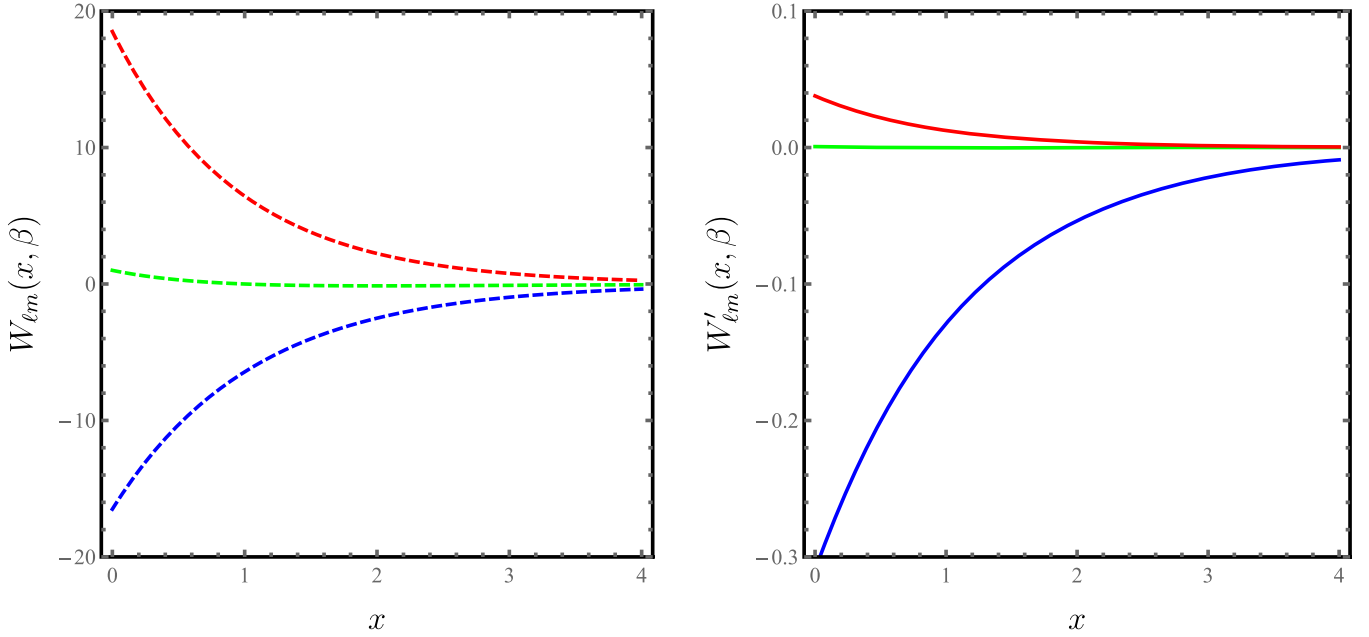
Figure 7. Torque weight functions for the smooth and scarred Mestel disks. Parameter values are the same as in earlier figures. The dashed lines of the left panel are for the $W_{\ell m}(x, \beta)$ of Equation (87). The solid lines in the right panel are for the $W'_{\ell m}(x, \beta)$ of Equation (93). Blue/green/red curves correspond to the ILR/CR/OLR, respectively.

we have $F_{fin}(J_f, J_s) \simeq F_{in}^{(0)} + (1/2)F_{in}^{(2)}(J_s - J_*)^2$. Hence, the integrand is

$$\frac{\partial F_{fin}}{\partial J_s}\delta(\Omega'_s)|\widehat{\Psi}_{\ell m}(J_f, J_s)|^2$$

$$= F_{in}^{(2)}(J_s - J_*)\frac{\delta(J_s - J'_*)}{|B_*|}[1 - \delta_{\ell m}]|\widehat{\Psi}_{\ell m}(J_f, J_s)|^2$$

$$= F_{in}^{(2)}(J'_* - J_*)\frac{\delta(J_s - J'_*)}{|B_*|}[1 - \delta_{\ell m}]|\widehat{\Psi}_{\ell m}(J_f, J'_*)|^2.$$

From Equation (82), we have $J'_* - J_* \simeq -(\delta_{\ell m}/2)J_*$. Also, $\widehat{\Psi}_{\ell m}(J_f, J'_*) = \widehat{\Psi}_{\ell m}(J_f, J_*) + O(\delta_{\ell m})$. Therefore, to first order in $\delta_{\ell m}$, the integrand is given by

$$F_{in}^{(2)}\left[-\frac{1}{2}\delta_{\ell m}J_*\right]\frac{\delta(J_s - J'_*)}{|B_*|}|\widehat{\Psi}_{\ell m}(J_f, J_*)|^2. \quad (90)$$

Substituting Equation (90) into Equation (89), and integrating over J_s, the torque in the scarred Mestel disk is

$$\mathcal{T}'_{\ell m} \simeq -8\pi^3\varepsilon_s^2 m^2(-\delta_{\ell m}/2)$$

$$\times \int_{-\ell J_*}^{\infty} dJ_f \frac{J_* F_{in}^{(2)}(J_f)}{|B_*|}|\widehat{\Psi}_{\ell m}(J_f, J_*)|^2.$$

This is similar in form to $\mathcal{T}_{\ell m}$ of Equation (85), the torque in the smooth Mestel disk. The difference is that the integral has acquired a prefactor $(-\delta_{\ell m}/2)$, and $J_* F_{in}^{(2)}$ has replaced $F_{in}^{(1)}$ in the integrand. Because $|\delta_{\ell m}| \ll 1$, we can guess that $|\mathcal{T}'_{\ell m}| \ll |\mathcal{T}_{\ell m}|$. But this needs to be established by calculating $F_{in}^{(2)}(J_f) = (\partial^2 F_{in}/\partial J_s^2)_{J_s=J_*}$ for the Mestel DF of

Equation (48):

$$F_{in}^{(2)}(J_f) = \frac{C}{mJ_*^3}\left[\left(\frac{\beta J_f}{mJ_*}\right)^2 - 4\left(\frac{\beta J_f}{mJ_*}\right) + 2\right]$$

$$\times \exp\left\{-\frac{\beta}{m}\left(\frac{J_f}{J_*} + \ell\right)\right\}. \quad (91)$$

Introducing the integration variable x used in the passage from Equation (85) to (86), we obtain

$$\mathcal{T}'_{\ell m} = 8\pi^3\varepsilon_s^2 \frac{mC}{\beta\Omega_p}\int_0^{\infty} dx W'_{\ell m}(x, \beta)|\psi_{\ell m}(x, \beta)|^2, \quad (92)$$

where

$$W'_{\ell m}(x, \beta) = \frac{\delta_{\ell m}}{2}\left\{\left[x - \frac{\beta\ell}{m}\right]^2 - 4\left[x - \frac{\beta\ell}{m}\right] + 2\right\}$$

$$\times \exp(-x) \quad (93)$$

is the torque weight function for the scarred Mestel disk, plotted in the right panel of Figure 7, at the principal resonances.

5.3.3. Torque Suppression Factor

We want to make quantitative estimates of how small $\mathcal{T}'_{\ell m}$ is compared to $\mathcal{T}_{\ell m}$; to this end, we define the torque suppression factor due to a scar, $\mathcal{S}_{\ell m} = \mathcal{T}'_{\ell m}/\mathcal{T}_{\ell m}$. Equation (92) for $\mathcal{T}'_{\ell m}$ is similar in form to Equation (86) for $\mathcal{T}_{\ell m}$. Both torques have the same function, $|\psi_{\ell m}(x, \beta)|^2$, in the integrand, which depends on the radial profile of the linear mode, $\Psi_1(R, \phi, t)$. As discussed earlier, this must be taken from either models of observational data or fits to numerical simulations. However, we do not need to know the detailed functional form of $|\psi_{\ell m}(x, \beta)|^2$ in order to

make a rough estimate of $\mathcal{S}_{\ell m}$. This is done below by exploiting some specific properties of the weight functions, $W_{\ell m}(x, \beta)$ of Equation (87) and $W'_{\ell m}(x, \beta)$ of Equation (93), for the smooth and scarred disks, respectively.

Both weight functions fall off exponentially with x, so smaller values of x contribute most to the integrals. As can be seen in Figure 7, $W_{\ell m}(x, \beta)$ and $W'_{\ell m}(x, \beta)$ are negative at the ILR and positive at the OLR, so the linear mode absorbs/emits angular momentum at the ILR/OLR, as expected. Moreover, both weight functions have qualitatively similar forms to functions of x, but $W'_{\ell m}$ is smaller than $W_{\ell m}$ by a factor of about 50 for the ILR and 500 for the OLR. Both weight functions are small at the CR, as expected, where $W'_{\ell m}$ is smaller than $W_{\ell m}$ by a factor of about 1000. Therefore, for $|\psi_{\ell m}(x, \beta)|^2$ of general form, $\mathcal{T}'_{\ell m}$ will be much smaller than $\mathcal{T}_{\ell m}$. Hence, a first estimate of the ratio of the torques is given by the ratio of their weight functions near $x \simeq 0$. Therefore, the torque suppression factor is:

$$\mathcal{S}_{\ell m} \sim \frac{W'_{\ell m}(0, \beta)}{W_{\ell m}(0, \beta)} = \frac{\delta_{\ell m}}{2} \frac{(\beta \ell/m)^2 + 4(\beta \ell/m) + 2}{(\beta \ell/m) + 1}. \quad (94)$$

Using the values for $\delta_{\ell m}$ in Equation (78), and $\beta = 35$ and $m = 2$ as earlier,

$$\mathcal{S}_{\ell m} \sim \{1.9 \times 10^{-2}, 7 \times 10^{-4}, 2 \times 10^{-3}\} \quad (95)$$

at the ILR, CR and OLR, respectively.

6. Renewal of Modes in the Scarred Disk

In Section 6.1, we first establish that the suppressed torques, exerted on the final disk by linear modes of the form $\Psi_1(R, \phi, t)$ of Equation (67), also imply that the heating of disk stars is much smaller in the final disk than in the initial disk. In contrast, for some other linear mode $\bar{\Psi}_1(R, \phi, t)$, with a different angular wavenumber or pattern speed, resonant torques and heating are generically comparable in the initial and final disks. In Section 6.2 we consider the implications of this for mode renewal in the final disk and compare with the simulations of SC14.

6.1. Suppressed Epicyclic Heating due to $\Psi_1(R, \phi, t)$

The epicyclic energies (per unit mass) of resonant stars change at the rates $\dot{\mathcal{E}}_{\rm epi} \simeq (\ell/m)\kappa_* \mathcal{T}_{\ell m}$ and $\dot{\mathcal{E}}'_{\rm epi} \simeq (\ell/m)\kappa'_* \mathcal{T}'_{\ell m}$ in the initial and final disks, respectively. Here, κ_* and κ'_* are the epicyclic frequencies at resonance. Both $\dot{\mathcal{E}}_{\rm epi}$ and $\dot{\mathcal{E}}'_{\rm epi}$ are positive at the ILR and OLR, and vanish at the CR. Because $|\mathcal{T}'_{\ell m}| \ll |\mathcal{T}_{\ell m}|$, we expect that $\dot{\mathcal{E}}'_{\rm epi} \ll \dot{\mathcal{E}}_{\rm epi}$. This is indeed true: as κ_* and κ'_* differ only by $O(\delta_{\ell m})$, to first order in $\delta_{\ell m}$, the ratio of the heating rates is

$$\frac{\dot{\mathcal{E}}'_{\rm epi}}{\dot{\mathcal{E}}_{\rm epi}} \simeq \frac{\mathcal{T}'_{\ell m}}{\mathcal{T}_{\ell m}} = \mathcal{S}_{\ell m} \ll 1. \quad (96)$$

Therefore, linear modes of the form $\Psi_1(R, \phi, t)$ of Equation (67) suffer much less collisionless dissipation in the final disk. This is entirely due to the fact that resonance shifts are small, $\sim O(\delta_{\ell m})$, so that the resonant lines lie within the scars of the final disk, where the final DF is flattened (as a function of J_s).

We now compare the torques in the initial and final disks, due to some other linear mode, $\bar{\Psi}_1(R, \phi, t)$:

$$\bar{\Psi}_1 = \varepsilon_s \exp(\gamma t) \bar{\Psi}_a(R) \cos\{\bar{m}(\phi - \bar{\Omega}_{\rm p} t) + \bar{\zeta}_a(R)\}, \quad (97)$$

where $\bar{m}$ and $\bar{\Omega}_{\rm p}$ can be different from m and $\Omega_{\rm p}$. Below we show that (i) the two sets of ILR/CR/OLR, for $\bar{\Psi}_1$ and Ψ_1, are well separated in the smooth and scarred Mestel disks. (ii) Generically, the ILR/CR/OLR of $\bar{\Psi}_1$ pass through scar-free regions of the final disk, so that resonant torques and heating due to $\bar{\Psi}_1$ will be nearly the same in both disks.

1. We first consider resonant lines, $(\ell, \bar{m})$ due to $\bar{\Psi}_1$ and (ℓ, m) due to Ψ_1 in the smooth Mestel disk. The latter is given as $J_s = J_*$ of Equation (42), where we will treat the parameters $(m, \Omega_{\rm p})$ as given and fixed. Similarly, the $(\ell, \bar{m})$ resonant line is $J_s = \bar{J}_*$, where

$$\bar{J}_* = \frac{V_0^2}{\bar{m}\bar{\Omega}_{\rm p}}\left[1 + \sqrt{2}\frac{\ell}{\bar{m}}\right]. \quad (98)$$

In order for the resonant lines of $\bar{\Psi}_1$ and Ψ_1 to be close to each other, $\bar{J}_* \simeq J_*$. For the CRs (i.e., $\ell = 0$), this implies that $\bar{m}\bar{\Omega}_{\rm p} \simeq m\Omega_{\rm p}$, a condition which can evidently be satisfied by many $\bar{m} \neq m$ and $\bar{\Omega}_{\rm p} \neq \Omega_{\rm p}$. In addition, if we require that the ILR and OLR also must coincide, $\bar{m} \simeq m$. Because $\bar{m}$ and m are positive integers, this can be satisfied only if $\bar{m} = m$ and $\bar{\Omega}_{\rm p} \simeq \Omega_{\rm p}$. Hence, for $\bar{m} \neq m$ or $\bar{\Omega}_{\rm p}$ significantly different from $\Omega_{\rm p}$, the $(\ell, \bar{m})$ and (ℓ, m) resonant lines will be well separated in phase space.

2. Next, we consider resonant lines, $(\ell, \bar{m})$ due to $\bar{\Psi}_1$ and (ℓ, m) due to Ψ_1 in the scarred Mestel disk. The latter is given as $J_s = J'_* = [1 - (\delta_{\ell m}/2)]J_*$, which we know lies well within the scar. Outside the scarred regions, the orbital and epicyclic frequencies are nearly the same in both disks (with small differences due to the dipolar fields of distant scars, discussed in Section 5.2.1). So, the $(\ell, \bar{m})$ resonant line in the scarred disk will nearly coincide with the $(\ell, \bar{m})$ line in the smooth disk.

3. From items 1 and 2 above, we conclude that the ILR/CR/OLR due to $\bar{\Psi}_1$ lie close to each other in the smooth and scarred disks, and that these must be well separated from the ILR/CR/OLR, due to Ψ_1. Hence, the $(\ell, \bar{m})$ line in the final disk generically traverses scar-free regions of phase space,[10] where the DF near it is given by the smooth Mestel DF of Equation (38), the resonant torques exerted by a marginally growing $\bar{\Psi}_1$ are nearly the same for the smooth and scarred Mestel disks, and given by

$$\bar{\mathcal{T}}_{\ell\bar{m}} = 8\pi^3\varepsilon_s^2 \frac{\bar{m}C}{\beta\bar{\Omega}_{\rm p}} \int_0^\infty dx W_{\ell\bar{m}}(x, \beta)|\bar{\psi}_{\ell\bar{m}}(x, \beta)|^2, \quad (99)$$

where $W_{\ell\bar{m}}(x, \beta)$ is the same as in Equation (87) with m replaced by $\bar{m}$, and $\bar{\psi}_{\ell\bar{m}}(x, \beta)$ is the Fourier coefficient corresponding to $\bar{\Psi}_1$. Equivalently, we can think of the torque suppression factor, $\bar{\mathcal{S}}_{\ell\bar{m}} \sim 1$. From Equation (96), the ratio of the heating rates in the final and initial disks is $\sim \bar{\mathcal{S}}_{\ell\bar{m}} \sim 1$, so $\bar{\Psi}_1$

---

[10] We note the possibility that a particular $(\ell, \bar{m})$ resonant curve of $\bar{\Psi}_1$ might pass through some scar, while other $(\ell', \bar{m})$ resonant curves of $\bar{\Psi}_1$ (with $\ell' \neq \ell$) lie in scar-free regions. We assume that this is not the case, but that does not mean that such an "accidental overlap" of a single resonant line with a single scar is uninteresting. Indeed, it might well prove important, but this problem is beyond the scope of this paper.

can be expected to cause comparable amounts of heating in both disks.

6.2. Model of Mode Renewal

In numerical simulations of smooth stellar disks, sampling shot noise generates a spectrum of spiral modes, some of which grow to somewhat large amplitudes and decay through absorption at the Lindblad resonances. Let us consider one of these transient spiral modes, with angular wavenumber m and pattern speed $\Omega_{\rm p}$. It will transform an initially smooth disk into a scarred disk, whose main scars are at the ILR/CR/OLR. Spiral modes generated by shot noise in the scarred disk will behave differently. In Section 6.1, we showed that the resonant torque and heating suppression factor $\mathcal{S}_{\ell m} \ll 1$ for linear modes, Ψ_1, with the the same $(m, \Omega_{\rm p})$ as the precursor transient mode. But for a linear mode $\bar{\Psi}_1$ with different $(\bar{m}, \bar{\Omega}_{\rm p})$, $\bar{\mathcal{S}}_{\ell \bar{m}} \sim 1$ for all ℓ, except in the case of accidental overlaps mentioned in footnote 10. Hence, among the spectrum of modes generated by shot noise, modes like Ψ_1—which suffer far less dissipation than other modes like $\bar{\Psi}_1$—will grow to larger amplitudes and dominate the renewed spiral pattern. We may think of the scars as filtering a noisy generator.

There appears to be some support for this model of mode renewal in the simulations of SC14. Their Figure 5 plots the power in modes $m = 2, 3, 4$ as functions of radius and frequency. The top panels correspond to transient modes that scar the disk, and the bottom panels are for modes that are regenerated in the scarred disk. The central panels are for the $m = 3$ mode, which show that the renewed mode has the same frequency as its precursor. Moreover, their spatial forms, displayed in panels (c) and (f) of Figure 6, are also strikingly similar. But the interpretation is not so clean, because of the presence of large-amplitude $m = 2, 4$ modes; this is briefly discussed in Section 7.

SC14's (p. 1) physical picture of mode renewal is presented in the "local" picture of wave-packet behavior near Lindblad resonances:

"The scattering of stars as each wave decays takes place over narrow ranges of angular momentum, causing abrupt changes to the impedance of the disk to subsequent traveling waves. Partial reflections of waves at these newly created features allows new standing-wave instabilities to appear that saturate and decay in their turn, scattering particles at new locations, creating a recurring cycle."

In the "global" LBK approach of our paper, the "narrow ranges of angular momentum" would correspond to the narrow scars surrounding resonant curves in phase space; the "abrupt changes to the impedance of the disk to subsequent traveling waves" can be thought of as the abrupt flattening of the final DF (as a function of the slow action) across a scar; and the "partial reflection of waves..." would be due to the suppressed dissipation within scars. The renewed modes in our model would then correspond to the cavity-type "mirror modes" described by SC14, which are sustained by swing amplification at the CR and partial reflection at the scar of a Lindblad resonance.

The partial reflection must, as SC14 realize, arise from a modification near the Lindblad resonances of the WKB dispersion relation for spiral density waves. We can think of this in the following manner. The standard Lin–Shu–Kalnajs dispersion relation for stellar disks (Lin & Shu 1966; Binney & Tremaine 2008) is valid for the smooth initial DF. In order to study the reflection of waves in the scarred disk, it is necessary

to derive a dispersion relation for spiral wave packets in the final disk. Because our final DF is equal to the initial DF outside scars and flattened within, we may expect the new dispersion relation to be different from the old one only near resonances. This can be worked out; indeed, it is necessary to supplement our "global" LBK approach with a "local" picture of wave-packet propagation between the corotation and Lindblad resonances. Only then will we understand weak torques, suppressed dissipation, and mode renewal in terms of spiral density waves that are partially reflected at the Lindblad resonances. What may we expect of such a modified LSK dispersion, based on the results of Sections 5 and 6.1? In Section 5.1, we showed that, when the self-gravity of the scars is ignored (i.e., when $\delta_{\ell m} = 0$), the resonant torques vanish, and there is no dissipation. In the corresponding local picture, the encounter of a wave packet with a resonant scar must be lossless, so reflection should be perfect. When self-gravity is included (i.e., when $\delta_{\ell m} \neq 0$), the resonant torques and dissipation are suppressed but not zero, as we showed in Section 6; this more generic case should correspond to the partial reflection of a wave packet.

SC14 also observed that each cycle of mode renewal heats up the disk until $Q \gtrsim 2$, when it becomes less responsive. This fact is also consistent with our picture of suppressed dissipation of certain linear modes of the form Ψ_1. This is because, in our model of mode renewal as a noise-filtering process, the lower dissipation rates of these modes enable them to grow to greater amplitudes than other linear modes $\bar{\Psi}_1$. But the decay of these, by now, large-amplitude modes would be governed by nonlinear effects; SC14's simulations appear to suggest that the nonlinear decay timescales may be comparable in the initial and final disks, but this remains to be investigated. We suggest that the filtering action of scars, operating on noise-generated modes when their amplitudes are still small enough to be "linear," is the basic physical mechanism regulating mode renewal.

7. Conclusions

We presented a model of the renewal of nonaxisymmetric modes in stellar disks that have experienced the passage of a small-amplitude, transient nonaxisymmetric mode with angular wavenumber m and pattern speed $\Omega_{\rm p}$. The physical mechanism relies on the nonlinear readjustment of the phase-space distribution of stars in the vicinity of resonances, which can be thought of as scars left behind by the transient mode. The DF of the final disk is flattened (as a function of the slow action) within narrow scars, resulting in the suppression of resonant torques and epicyclic heating. In particular, linear modes with the same $(m, \Omega_{\rm p})$ as the transient mode that produced the final disk from the initial disk transport much less angular momentum, and suffer much less dissipation, than other linear modes with different angular wavenumbers or pattern speeds. Therefore, the set of resonant scars acts as a filter of the spectrum of linear modes generated by shot noise in numerical simulations, promoting the preferential growth of linear modes with the same $(m, \Omega_{\rm p})$. These then grow to large amplitudes and dominate the appearance of the disk. Their subsequent decay would depend on nonlinear processes that are not considered in this paper, and decay timescales could be comparable in the initial and final disks. As the disk eventually heats up and becomes less responsive, some form of cooling is necessary for recurrent spiral activity; accretion of cold gas and

new star formation have been thought of as the main physical agents, and we have little to add to this.

The renewed modes we identified correspond to the cavity-type mirror modes of SC14. In the local picture of wave-packet propagation, these can be thought of as spiral density waves that are swing-amplified at corotation and partially reflected at a Lindblad resonance in a scarred disk. These two physical ingredients have been emphasized recently by Binney (2019): "The swing amplifier and resonant absorption are the stand-out pieces of physics in this beautiful mechanism by which galaxies like ours evolve." Whereas the swing amplifier is reasonably well understood, resonant absorption in scars has not received much attention. Our study of the physics of resonant absorption from a global LBK point of view has revealed that it can be highly suppressed within scars. We also noted that this should imply partial reflection of wave packets in the local description, whose quantitative description should come from a modified LSK dispersion relation near scars, giving rise to abrupt changes in the impedance of the disk proposed by SC14.

The final DF for the scarred Mestel disk of Section 4.4.1 could be used for initial conditions in simulations to test our model of mode renewal. This will help clarify matters in at least two ways:

a. Our discussion of noise-generated modes in a scarred disk was based on simulations. The physical kinetics of the generation of phase structures, such as ridges in action space, from the discreteness of unscarred disks has been explored by Fouvry et al. (2015a, 2015b). To study the filtering action of scars we have proposed, it is necessary to extend the theory to scarred disks. The theory could then be compared with controlled simulations of the scarred Mestel disk.

b. As support for our model, we cited the case of the renewal, recurrence even, of an $m = 3$ mode in the simulations of SC14, while noting that the interpretation is confused by the presence of $m = 2, 4$ modes. SC14 state that these two modes are not independent, so it is plausible that there is some overlap in the sets of scars produced by the $m = 2, 3, 4$ precursor modes and nonlinear interactions among the modes. In the SC14 simulations, what we have referred to as the scarred disk was produced from the smooth disk through the action of a superposition of transient spiral and bar-like modes, of which $m = 2, 3, 4$ are the most prominent. Using the scarred Mestel disk would provide a cleaner initial condition.

Sellwood & Carlberg (2019) present numerical experiments on mode recurrence in disks seeded by a groove scored by hand. The groove gives rise to an $m = 2$ instability, which is not a cavity-type mode (Sellwood & Lin 1989; Sellwood & Kahn 1991). This "groove mode" is transient, and its decay leaves behind scars at the principal resonances, as given in their Figure 6. The sense of mass shifts across resonant lines appears to be consistent with what is expected from our Section 4.4.1; Figure 7 of their paper is essentially the DF of the OLR scar (when due allowance is made for the finite slopes of the resonant lines—see our footnote 7 of Section 4.1). Two new $m = 2$ modes are then generated by the scars of the transient precursor groove mode. The weaker of the two renewed modes has the same frequency as the precursor (lines 4 and 6 of their Table 2) and is likely to be a cavity-type mirror mode of the sort we discussed. But the stronger mode has a lower frequency than the precursor groove mode (lines 2, 3, and 5 of their Table 2), so it is not a

cavity mode of the type we considered. However, its CR passes through the OLR scar of the precursor, implying that its Lindblad resonances would pass through unscarred parts of the disk. This may correspond to a case of "accidental overlap," mentioned in footnote 10 of our Section 6.1 but not discussed further.

We considered a precursor transient mode with fractional surface density perturbation, $\varepsilon_d = 10^{-2}$, but this can be increased to $\varepsilon_d = 10^{-1}$, which is closer to simulations, as argued below.[11] Because the filtering action of scars arises from the flattening of the DF within scars, the resonance shifts, δJ_* of Equation (84), must be smaller in magnitude than ΔJ, the half-width of the scar. For $\varepsilon_d = 10^{-2}$, we have $|\delta J_*|/\Delta J \sim 10^{-2}$ (for an $m = 2$ mode), so resonant lines in the scarred disk pass through the very central regions of the scar. Because $\delta J_* \propto \varepsilon_d^{3/2}$ and $\Delta J \propto \varepsilon_d^{1/2}$, we expect $|\delta J_*|/\Delta J \sim \varepsilon_d$. Hence, for $\varepsilon_d = 10^{-1}$, which is closer to simulations, $|\delta J_*|/\Delta J \sim$ few $\times 10^{-1}$. The resonant lines still sample the flattened regions within scars, so Equation (94) for $\mathcal{S}_{\ell m}$, the torque (and dissipation) suppression factor, would be valid. From Equation (95), $\mathcal{S}_{\ell m} \sim 10^{-2} - 10^{-3}$ at the principal resonances for $\varepsilon_d = 10^{-2}$. Because $\mathcal{S}_{\ell m} \propto \varepsilon_d^{3/2}$, for $\varepsilon_d = 10^{-1}$, we have $\mathcal{S}_{\ell m} \sim 0.03 - 0.3$. Resonant torques and dissipation are larger, but the filtering action of scars might still be expected to work for this more realistic transient mode.

There is room for further improvement in the calculations presented here, for closer comparisons with simulations or confrontation with observational data. We assumed that the growth and decay times of the transient mode were large enough that we could calculate the form of a scar in the adiabatic limit. But the transient modes in simulations are faster, so we need to extend our calculations beyond the adiabatic limit. The passage of a nonadiabatic transient will result in greater mixing of the initially axisymmetric DF. This will produce a scarred disk that is nonaxisymmetric, unlike the adiabatically scarred disk we have considered in this paper. The nonaxisymmetry is of interest, in itself, but it does not seem to affect mode renewal, as has been tested in simulations by starting reruns after randomizing in ϕ at fixed R, p_R, and p_ϕ (see, e.g., Sellwood & Lin 1989; Sellwood 2012). So, we can focus on the axisymmetric part of the scars and ask how different these are from the adiabatic scars of this paper; the more vigorous stirring would smoothen the boundaries, but the interesting questions would relate to DF changes near scar centers.

For explicit calculations involving scars in a cool Mestel disk, we replaced the functions $D_{\ell m}(J_f)$, determining the scar boundaries by resonance-dependent constants $\bar{D}_{\ell m}$. This proved a useful surrogate for the estimation of integrated quantities, providing results that are physically in line with expectations: the sense of mass shifts in phase space, the magnitudes and signs of the angular momentum absorbed during scar formation, and the shapes of $\Delta\Sigma_{\ell m}(R)$, which all determine

---

[11] The reason for not using the more realistic value, $\varepsilon_d = 10^{-1}$, straightaway is the following. Unless the pendulum approximation of Equation (22) itself needs improvement, we expect all the calculations up to and including Section 4.4.1 would remain unchanged. But the formula for the surface density of scars, $\Delta\Sigma_{\ell m}(R)$ of Equation (63), would be modified. This was derived in Appendix B.1 by assuming that $\Delta R/R_{epi} \ll 1$. From Equation (61), this is a $\sim$ few $\times 10^{-1}$ for $\varepsilon_d = 10^{-2}$. Because $\Delta R/R_{epi} \propto \varepsilon_d^{1/2}$, this ratio is ~ 1 for $\varepsilon_d = 10^{-1}$. Then $\Delta\Sigma_{\ell m}(R)$, the radial acceleration due to scars, $\Delta a_{\ell m}(R)$, and subsequent development, would require the use of special functions and integrals over them. It was felt that presenting these as such would have obscured the physics.

the subsequent development. But it is a poor representation of the scar boundaries and not suitable for comparison with observational data. Indeed, the functions $D_{\ell m}(J_f)$ can be calculated for any assumed radial profile for the transient. It is necessary to do this, were one to search for transient spiral activity in our Galaxy in *Gaia*DR2, such as Trick et al. (2019) for axisymmetric features and Sellwood et al. (2017) and Monari et al. (2019) for nonaxisymmetric features.

Coherent and symmetric spiral patterns are often seen in barred galaxies, or galaxies that have been tidally perturbed by interaction with a passing companion galaxy (Kormendy & Norman 1979; Kendall et al. 2011). Because the spiral has a lower pattern speed than the bar (Sellwood & Sparke 1988), this is a more complicated—and very interesting—problem than we considered, involving two pattern speeds. The tidal perturbation poses a different sort of problem, because the tidal potential does not have a well-defined pattern speed. But it drives a large-scale spiral pattern in the galaxy with a strong $m = 2$ component that would eventually decay. If the tidally driven spiral behaves somewhat like the transient modes of this paper, relic scars left behind by its passage could enable the renewal of patterns resembling "grand design" spirals. Further extension of our model, guided by simulations, is required to address these problems.

Appendix A
Final DF after the Passage of the Adiabatic Transient

We use ST96 to follow the time evolution of the initial DF, $F_{in}(J_f, J_s)$ of Equation (24), due to an adiabatic transient mode with time profile function $A(\tau)$ that is nonzero only between $\tau_<$ and $\tau_>$: $A(\tau)$ increases monotonically from zero at $\tau_<$, reaches a maximum value of unity at τ_0, and then decreases monotonically to zero at $\tau_>$. The τ-evolving DF is followed as a function of the fast action J_f and the "adiabatic invariant" K of Equation (25), and the final DF of Equation (27) is derived.

ST96 is valid for Hamiltonians of more general form than H, for which $C_\pm$ can be asymmetric and expand or contract at different rates. As given in Table 1 of ST96, there are altogether six cases of separatrix crossings to consider. But, for the H of Equation (22), $C_\pm$ are always reflection-symmetric about $J_s = J_*$, so the number of cases reduces to two; see items 2 and 5 below.

It is convenient to use separate notations for trapped orbits (in region II) and circulating orbits (in regions I and III). In II, $K = 0$ for the elliptic fixed point orbit. For the limiting librating orbit, $H \to E_{sx}$ just inside $C_\pm$, we can calculate $K = \mathcal{K}$ using Equation (23):

$$\mathcal{K}(\tau; J_f) = \frac{2}{\pi} \sqrt{\frac{E_{sx}}{B_*}} \int_{\xi_* - \pi}^{\xi_* + \pi} d\theta_s \cos\{(\theta_s - \xi_*)/2\}$$
$$= \frac{8}{\pi} \sqrt{\frac{\varepsilon_p A(\tau) \Phi_*}{B_*}} \geqslant 0. \quad (100)$$

K is discontinuous across $C_\pm$, because the pendulum phase space is divided. We use $K = K_a$ to describe the trapped orbits of region II and $K = K_b$ to describe the circulating orbits of regions I and III. The time-evolving DF is written as F_a in II

and F_b in I and III:

$F_a(K_a, \tau; J_f)$ for $0 \leqslant K_a < \mathcal{K}(\tau; J_f)$
    (trapped orbits in II),   (101a)

$F_b(K_b, \tau; J_f)$ for

$$\begin{cases} K_b \leqslant -\dfrac{1}{2} K(\tau; J_f) & \text{(circulating orbits in I)} \\[2mm] K_b \geqslant +\dfrac{1}{2} K(\tau; J_f) & \text{(circulating orbits in III)} \end{cases} \quad (101b)$$

As $A(\tau)$ grows and decays, the range of values taken by the variables, K_a and K_b, varies with τ. Within these shifting boundaries, the functional forms of the DFs, F_a and F_b, also change with τ. Below we follow the time evolution of F_a and F_b through seven simple steps and determine the final DF.

1. Initial state: $A = 0$ at $\tau_<$, so both $C_\pm$ collapse to the line $J_s = L_*$ and $\mathcal{K} = 0$. There are no trapped orbits, so we can ignore both K_a and F_a. For the circulating orbits, we know from Section 3.2 that $K_b = J_s - J_*$. Then,

$$F_b(K_b, \tau_<; J_f) = F_{in}(J_f, J_* + K_b). \quad (102)$$

2. Expansion: As $A(\tau)$ increases, circulating orbits encountering the expanding $C_\pm$ are trapped into librating orbits. Let us pick a time τ_1 between $\tau_<$ and τ_0.

 a. Because orbits in regions I and III (defined at τ_1) have not experienced separatrix crossing, K_b is an adiabatic invariant, so F_b retains the same form as Equation (102):

$$F_b(K_b, \tau_1; J_f) = F_{in}(J_f, J_* + K_b),$$
$$\text{for } |K_b| \geqslant \frac{1}{2} K_1, \quad (103)$$

 where $K_1 = \mathcal{K}(\tau_1; J_f)$.

 b. All of the trapped orbits with $0 \leqslant K_a < K_1$ have experienced separatrix crossing. We need F_a for the limiting librating orbit, $K_a \to K_1$, just inside $C_\pm$. Because $C_\pm$ expand symmetrically, according to case c of Table 1 in ST96, F_a contains equal proportions of F_b at $K_b = \pm K_1/2$:

$$F_a(K_a \to K_1, \tau_1; J_f) = \frac{F_b(K_1/2, \tau_1; J_f) + F_b(-K_1/2, \tau_1; J_f)}{2}$$
$$= \frac{F_{in}(J_f, J_* + K_1/2) + F_{in}(J_f, J_* - K_1/2)}{2}, \quad (104)$$

 where we have used Equation (103) to write the last equality.

3. Further expansion: As $A(\tau)$ increases, $C_\pm$ expand and trap orbits with $K_a > K_1$. Meanwhile, the value of the DF at K_1 remains frozen:

$$F_a(K_1, \tau; J_f) = F_a(K_a \to K_1, \tau_1; J_f)$$
$$= \frac{F_{in}(J_f, J_* + K_1/2) + F_{in}(J_f, J_* - K_1/2)}{2}. \quad (105)$$

4. Maximal expansion: Region II is maximal at τ_0 when $A = 1$. The orbits in I and III (defined at τ_0) do not ever experience separatrix crossing. For these, F_b at the final time is the same as that at the initial time. Using Equation (102), we

have

$$F_b(K_b, \tau_>; J_{\rm f}) = F_b(K_b, \tau_<; J_{\rm f}) = F_{\rm in}(J_{\rm f}, J_* + K_b)$$
$$\text{for } |K_b| \geqslant \Delta J(J_{\rm f}), \tag{106}$$

where

$$\Delta J(J_{\rm f}) = \frac{1}{2}\mathcal{K}(\tau_0; J_{\rm f}) = \frac{4}{\pi}\sqrt{\frac{\varepsilon_{\rm p}\Phi_*}{B_*}} > 0. \tag{107}$$

Below we calculate $F_b(K_b, \tau_>; J_{\rm f})$ for $|K_b| < \Delta J(J_{\rm f})$.

5. Contraction: For $\tau > \tau_0$, $A(\tau)$ is a decreasing function of τ, and $\mathcal{C}_\pm$ contract. Trapped orbits encountering the contracting $\mathcal{C}_\pm$ are liberated into circulating orbits. Let τ_2 be the (unique) time between τ_0 and $\tau_>$, when $A(\tau_2) = A(\tau_1)$. At this time, $0 \leqslant K_a < K_1$, and $|K_b| \geqslant K_1/2$, just like at τ_1 in item 2 above. According to case f of Table 1 in ST96, F_b at $K_b = \pm K_1/2$ (in III and I, respectively) is equal to $F_a(K_a{\rightarrow}K_1, \tau_2; J_{\rm f})$, which is the DF of the limiting trapped orbit at this time. Because the trapped orbit with $K_a = K_1$ has not experienced separatrix crossing during the interval $\tau_1 < \tau < \tau_2$, its DF has remained frozen in the form given by Equation (105). Then,

$$F_b(\pm K_1/2, \tau_2; J_{\rm f}) = F_a(K_a \rightarrow K_1, \tau_1; J_{\rm f})$$
$$= \frac{F_{\rm in}(J_{\rm f}, J_* + K_1/2) + F_{\rm in}(J_{\rm f}, J_* - K_1/2)}{2}. \tag{108}$$

6. Further contraction: As $A(\tau)$ decreases further, $\mathcal{C}_\pm$ shrink and the circulating orbits at $K_b = \pm K_1/2$ (in III and I, respectively) no longer experience any separatrix crossing. Hence, for all $\tau > \tau_2$, $F_b(\pm K_1/2, \tau; J_{\rm f}) = F_b(\pm K_1/2, \tau_2; J_{\rm f})$ remains frozen at the value given by Equation (108). We now note that, in item 2, we could have chosen τ_1 to take any value between $\tau_<$ and τ_0. So, K_1 can take any value between 0 and $2(\Delta J)$. Hence,

$$F_b(K_b, \tau_>; J_{\rm f}) = \frac{F_{\rm in}(J_{\rm f}, J_* + K_b) + F_{\rm in}(J_{\rm f}, J_* - K_b)}{2} \tag{109}$$
$$\text{for } |K_b| < \Delta J(J_{\rm f}).$$

7. Final state: Because $A(\tau_>) = 0$, just like the initial state, there are no trapped orbits. The circulating orbits are described by the F_b of Equations (106) and (109). Similar to the initial state, we have $K_b = J_{\rm s} - J_*$ in the final state. Substituting this into Equations (106) and (109), we obtain Equation (27) for the final DF.

Appendix B
Physical Quantities for a Scar in a Cool Mestel Disk

B.1. Surface Density

Here we derive Equation (63) for $\Delta\Sigma_{\ell m}(R)$ by using Equation (56) for $\Delta F_{\ell m}(J_R, L_z)$ in Equation (58). This is done in the small scar-width limit $\Delta R \ll R_{\rm epi} \ll R_*$, which is equivalent to $\Delta L \ll V_0 R_{\rm epi} \ll L_*$. Then, $\Delta F_{\ell m}(J_R, L_z) = 0$ for $|L_z - L_*| \geqslant \Delta L$, and for $|L_z - L_*| < \Delta L$,

$$\Delta F_{\ell m}(J_R, L_z) \simeq \frac{C}{L_*^2}\left[1 + \beta\frac{\ell}{m} - \beta\frac{J_R}{L_*}\right]$$
$$\times \exp\left\{-\beta\frac{J_R}{L_*}\right\}(L_z - L_*). \tag{110}$$

In the small scar-width limit,

$$J_R \simeq \frac{p_R^2}{2\kappa_*} + \frac{\kappa_*}{2}[R - R_{\rm g}(L_z)]^2, \tag{111}$$

where $\kappa_* = \sqrt{2}\,V_0^2/L_*$ is the epicyclic frequency at resonance. We can use this in Equation (110) to express $\Delta F_{\ell m}$ as a function of (R, p_R, L_z), which is the form required to calculate

$$\Delta\Sigma_{\ell m}(R) = \frac{1}{R}\int_{L_*-\Delta L}^{L_*+\Delta L} dL_z \int_{-\infty}^{\infty} dp_R\,\Delta F_{\ell m}. \tag{112}$$

The integral over p_R involves Gaussian-type integrals and is readily calculated. Then,

$$\Delta\Sigma_{\ell m}(R) = \frac{\sqrt{2\pi\sigma_0^2}\,C}{RL_*^2}\int_{L_*-\Delta L}^{L_*+\Delta L} dL_z(L_z - L_*)$$
$$\times\left[\frac{1}{2} + \beta\frac{\ell}{m} - \frac{\beta}{\sqrt{2}}\left(\frac{L_z - V_0 R}{L_*}\right)^2\right]$$
$$\times\exp\left\{-\frac{\beta}{\sqrt{2}}\left(\frac{L_z - V_0 R}{L_*}\right)^2\right\}. \tag{113}$$

This integral can be evaluated in terms of special functions, but we do not need them in the small scar-width limit. Because the integrand is a smooth function, it can be expanded in a Taylor series about $L_z = L_*$, where it can be seen that the lowest-order contribution comes from the $(L_z - L_*)^2$ term. Integrating this gives

$$\Delta\Sigma_{\ell m}(R) = \frac{\sqrt{2\pi\sigma_0^2}\,C}{R}\sqrt{2}\,\beta\left(\frac{R - R_*}{R_*}\right)$$
$$\times\left[\frac{3}{2} + \beta\frac{\ell}{m} - \frac{\beta}{\sqrt{2}}\left(\frac{R - R_*}{R_*}\right)^2\right]$$
$$\times\exp\left\{-\frac{\beta}{\sqrt{2}}\left(\frac{R - R_*}{R_*}\right)^2\right\}\frac{2}{3}\left(\frac{\Delta L}{L_*}\right)^3. \tag{114}$$

The surface density of a scar is $\propto (\Delta L)^3 \propto \varepsilon_{\rm d}^{3/2}$. $\Delta\Sigma_{\ell m}(R)$ is concentrated about R_* and becomes small for $|R - R_*| \gg R_{\rm epi}$, because of the Gaussian factor. Using the definitions of the constants C, σ_0, $R_{\rm epi} \simeq 2^{-1/4}\beta^{-1/2}\,R_*$, and Equation (57) for ΔL, we obtain $\Delta\Sigma_{\ell m}(R)$ as given in Equation (63).

B.2. Radial Acceleration

Here we derive Equation (76) by substituting the $\Delta\Sigma_{\ell m}(R)$ of Equation (63) into Equation (75):

$$\Delta a_{\ell m}(R) \simeq 2G\mu_{\ell m}\Sigma_0(R_*)\int_0^\infty \frac{dR'}{R' - R}\frac{R_*}{R'}\left(\frac{R' - R_*}{R_{\rm epi}}\right)$$
$$\times\left[1 - \frac{1}{3 + 2\beta(\ell/m)}\left(\frac{R' - R_*}{R_{\rm epi}}\right)^2\right]\exp\left\{-\frac{1}{2}\left(\frac{R' - R_*}{R_{\rm epi}}\right)^2\right\}. \tag{115}$$

Changing to a dimensionless integration variable, $x = (R' - R_*)/R_{\rm epi}$ and using $x_0 = (R - R_*)/R_{\rm epi}$,

$$\Delta a_{\ell m}(R) \simeq \frac{\mu_{\ell m}}{Q\sqrt{\beta}} \frac{V_0^2}{R_*}\left[\mathcal{I}_1(x_0) - \frac{\mathcal{I}_2(x_0)}{3 + 2\beta(\ell/m)}\right], \quad (116)$$

where

$$\mathcal{I}_1(x_0) = \int_{-(R_*/R_{\rm epi})}^{\infty} \frac{dx}{x - x_0} \frac{xe^{-x^2/2}}{[1 + (R_{\rm epi}/R_*)x]},$$

$$\mathcal{I}_2(x_0) = \int_{-(R_*/R_{\rm epi})}^{\infty} \frac{dx}{x - x_0} \frac{x^3 e^{-x^2/2}}{[1 + (R_{\rm epi}/R_*)x]}. \quad (117)$$

Because the Gaussian decays rapidly for $|x| > 1$ and $R_*/R_{\rm epi} \gg 1$, the lower limits of integration can be taken as $-\infty$ and $[1 + (R_{\rm epi}/R_*)x]^{-1} \simeq [1 - (R_{\rm epi}/R_*)x]$. Then,

$$\mathcal{I}_1(x_0) \simeq \int_{-\infty}^{\infty} \frac{dx}{x - x_0}[1 - (R_{\rm epi}/R_*)x]xe^{-x^2/2},$$

$$\mathcal{I}_2(x_0) \simeq \int_{-\infty}^{\infty} \frac{dx}{x - x_0}[1 - (R_{\rm epi}/R_*)x]x^3 e^{-x^2/2} \quad (118)$$

can be written in terms of special functions. But we require $\mathcal{I}_1(x_0)$ and $\mathcal{I}_2(x_0)$ only to first order in x_0:

$$\mathcal{I}_1(x_0) \simeq \mathcal{I}_2(x_0) \simeq \sqrt{2\pi}\left[1 - \frac{R_{\rm epi}}{R_*}x_0 + O(x_0^2)\right]. \quad (119)$$

Substituting this in the above formula for $\Delta a_{\ell m}(R)$ gives Equation (76).

References

Athanassoula, E. 1984, PhR, 114, 321
Bertin, G., & Lin, C. C. 1996, Spiral Structure in Galaxies (Cambridge, MA: MIT Press)
Binney, J. 2013, in XXIII Canary Islands Winter School of Astrophysics, Secular Evolution of Galaxies, ed. J. Falcón-Barroso & J. H. Knapen (Cambridge: Cambridge Univ. Press), 259
Binney, J. 2019, MNRAS, submitted (arXiv:1906.11696)
Binney, J., & Tremaine, S. 2008, Galactic Dynamics (2nd ed.; Princeton, NJ: Princeton Univ. Press)

Carlberg, R. G., & Sellwood, J. A. 1985, ApJ, 292, 79
Chirikov, B. V. 1979, PhR, 52, 263
Evans, N. W., & Read, J. C. A. 1998, MNRAS, 300, 106
Fouvry, J.-B., Binney, J., & Pichon, C. 2015a, ApJ, 806, 117
Fouvry, J.-B., Pichon, C., Magorrian, J., & Chavanis, P. H. 2015b, A&A, 584, 129
Goldreich, P., & Lynden-Bell, D. 1965, MNRAS, 130, 125
Goldreich, P., & Peale, S. 1966, AJ, 71, 425
Hockney, R. W., & Brownrigg, D. R. K. 1974, MNRAS, 167, 351
James, R. A., & Sellwood, J. A. 1978, MNRAS, 182, 331
Julian, W. H., & Toomre, A. 1966, ApJ, 146, 810
Kalnajs, A. J. 1965, PhD thesis, Harvard Univ.
Kalnajs, A. J. 1971, ApJ, 166, 275
Kalnajs, A. J. 1977, ApJ, 212, 637
Kaur, K., & Sridhar, S. 2018, ApJ, 868, 134
Kendall, S., Kennicutt, R. C., & Clarke, C. 2011, MNRAS, 414, 538
Kormendy, J., & Norman, C. A. 1979, ApJ, 233, 539
Lin, C. C., & Shu, F. H. 1964, ApJ, 140, 646
Lin, C. C., & Shu, F. H. 1966, PNAS, 55, 229
Lynden-Bell, D., & Kalnajs, A. J. 1972, MNRAS, 157, 1
Mark, J. W.-K. 1974, ApJ, 193, 539
Miller, R. H., Prendergast, K. H., & Quirk, W. J. 1970, ApJ, 161, 903
Monari, G., Famaey, B., Fouvry, J.-B., & Binney, J. 2017, MNRAS, 471, 4314
Monari, G., Famaey, B., Siebert, A., Wegg, C., & Gerhard, O. 2019, A&A, 626, A41
Roškar, R., Debattista, V. P., Quinn, T. R., & Wadsley, J. 2012, MNRAS, 426, 2089
Sellwood, J. A. 1989, in Dynamics of Astrophysical Discs, ed. J. A. Sellwood (Cambridge: Cambridge Univ. Press), 155
Sellwood, J. A. 2012, ApJ, 751, 44
Sellwood, J. A. 2014, RvMP, 86, 1
Sellwood, J. A., & Binney, J. J. 2002, MNRAS, 336, 785
Sellwood, J. A., & Carlberg, R. G. 1984, ApJ, 282, 61
Sellwood, J. A., & Carlberg, R. G. 2014, ApJ, 785, 137
Sellwood, J. A., & Carlberg, R. G. 2019, MNRAS, 489, 116
Sellwood, J. A., & Kahn, F. D. 1991, MNRAS, 250, 278
Sellwood, J. A., & Lin, D. N. C. 1989, MNRAS, 240, 991
Sellwood, J. A., & Sparke, L. S. 1988, MNRAS, 231, 25P
Sellwood, J. A., Trick, W. H., Carlberg, R. G., Coronado, J., & Rix, H.-W. 2017, MNRAS, 484, 3154
Shu, F. H. 2016, ARA&A, 54, 667
Sridhar, S., & Touma, J. 1996, MNRAS, 279, 1263
Toomre, A. 1969, ApJ, 158, 899
Toomre, A. 1977, ARA&A, 15, 437
Toomre, A. 1981, in Structure and Evolution of Normal Galaxies, ed. S. M. Fall & D. Lynden-Bell (Cambridge: Cambridge Univ. Press), 111
Trick, W. H., Coronado, J., & Rix, H.-W. 2019, MNRAS, 484, 3291